



PEOPLE'S DEMOCRATIC REPUBLIC OF ALGERIA
MINISTRY OF HIGHER EDUCATION AND SCIENTIFIC RESEARCH
UNIVERSITY OF MENTOURI BROTHERS, CONSTANTINE 1
FACULTY OF EXACT SCIENCES
PHYSICS DEPARTMENT

Order number:

Series:

MASTER'S THESIS

FIELD: MATERIAL SCIENCES

SECTOR: PHYSICS

SPECIALTY: NANOPHYSICS

THEME:

**STUDY OF THE PHOTOCATALYTIC ACTIVITY OF NANOMATERIALS
BASED ON METAL OXIDES SEMICONDUCTORS**

Presented by:

BARAMA Nail El Hocine

and

BOUKHECHE Khadidja

Presented on: 08 / 09 / 2020

Jury members:

President: M. SAHLI

Prof. University of Mentouri Brothers, Constantine 1

Reporter: M. SEBAIS

Prof. University of Mentouri Brothers, Constantine 1

Examiner: S. BOUDJADAR

Prof. University of Mentouri Brothers, Constantine 1

Acknowledgment

First, we thank the Almighty ALLAH for giving us the will and courage to do this work.

This work was carried out in the crystallography laboratory of the physics department, exact sciences faculty, University of Mentouri Brothers, Constantine 1.

We greatly thank Professor Mr. Miloud SEBAIS who entrusted us this work and kindly helped us. Big thanks for his patience and his availability.

We would like to express our great consideration and our sincere gratitude to M. SAHLI Professor at the University of Mentouri Brothers, Constantine 1 for having accepted to chair the jury of this master thesis.

We would like to thank professor S. BOUDJADAR from the University of Mentouri Brothers, Constantine 1 for accepting to judge the work of this Master's thesis.

We thank all the members of the crystallography laboratory and particularly MAMMERY Sabah, TOUAHRI Souad, and Saidi fayçal for the welcome, help, and provided advice.

We thank particularly Dr Leila BOUMAIZA for her help in XRD analysis of our powders.

In the end, we express our thanks to all those who contributed from far or near to the realization of this work.

To all, a big thanks you.

Dedications

This study is wholeheartedly dedicated to our beloved parents, who have been our source of inspiration and gave us strength when we thought of giving up, who continually provide their moral, spiritual, emotional, and financial support.

To our brothers, sisters, relatives, mentor, friends, and classmates who shared their words of advice and encouragement to finish this study.

Contents

paragraph		Page
I	General Introduction	1
II	Overview of Photocatalytic Depollution	3
II.1	Introduction	3
II.2	Principles of Heterogenous Photocatalysis	3
II.3	Radiation Sources for Photocatalysis	6
II.4	Factors Affecting the Degradation Performance	6
II.4.1	Catalyst Loading	6
II.4.2	PH of the Solution	7
II.4.3	Size and Structure of the Photocatalyst	7
II.4.4	Temperature Effect	7
II.4.5	Concentration and Nature of the Pollutants	8
II.5	Photocatalytic Semiconductors Classification	8
II.6	Nanocrystalline Photocatalysts	9
II.7	Cupric Oxide	10
III	Elaboration of Photocatalysts (Pure CuO and Sr Doped CuO)	12
III.1	Introduction	12
III.2	Elaboration of Pure CuO and Sr Doped CuO	12
III.2.1	Elaboration of Pure CuO Nanoparticles	12
III.2.2	Elaboration of Sr Doped CuO Nanoparticles	13
III.3	Washing	13
III.4	Drying	14
IV	Structural and Optical Characterization of Elaborated Photocatalysts (Pure CuO and Sr Doped CuO)	15
IV.1	Structural Characterization	15
IV.1.1	X-Ray Diffraction	15
IV.1.1.1	Identification of the formed phases	16
IV.1.1.2	Crystallites size	20

IV.1.1.3	Williamson-Hall deconvolution method	23
IV.1.1.4	Dislocations density in the produced CuO powders	25
IV.1.1.5	Specific surface of the nanoparticles	26
IV.1.2	Infrared Spectroscopy	28
IV.1.2.1	Introduction	28
IV.1.2.2	Infrared Analysis	28
IV.2	Optical characterization (UV-Visible Absorption)	31
IV.2.1	UV-Visible absorption spectra analysis	31
IV.2.2	Band Gap energy	33
V	Evaluation of Photocatalytic Activity of Elaborated Photocatalysts (Pure CuO and Sr Doped CuO)	38
V.1	Study of methylene blue photolysis	38
V.2	Study of adsorption effect of pure CuO and Sr doped CuO powders	39
V.3	Study of Photocatalytic Effect of Pure CuO and Sr Doped CuO powders	42
VI	General Conclusion	46
VII	References	48

I- General Introduction:

The impact of pollution on air and water, which are essential for the life of humans, animals and plants, is increasingly felt. To remedy this worrying situation, it is necessary to develop suitable and effective solutions and this is why in recent years, environmental pollution has become the focus of scientific world.

As one of the most promising solutions for these problems, photocatalysis has attracted much attention. Since the decomposition of water into hydrogen and oxygen on titanium electrode by Fujishima and Honda in 1972 [1], and it has been established as an efficient process for the mineralization of toxic organic compounds [2], dangerous inorganic constituents and bacteria disinfection [3] owing to the strong oxidizing agent, i.e. hydroxyl radical (OH•) [4].

Some metal oxide semiconductors like titanium dioxide (TiO₂), zinc oxide (ZnO), tungsten oxide (WO₃), strontium titanate (SrTiO₃) and hematite (Fe₂O₃) are proven to be dynamic photocatalysts [5]. However, most of these semiconductor photocatalysts have bandgap in the ultraviolet (UV) region, i.e., equivalent to or larger than 3.2 eV ($\lambda = 387$ nm). Therefore, they only promote photocatalysis upon illumination with UV radiation.

Besides, it has been estimated that the amount of solar energy reached on the Earth every day is more than that mankind could use for 30 years [6]. Unfortunately, in the whole energy of incoming solar spectrum, ultraviolet radiation ($\lambda < 400$ nm) accounts for only less than 4%, while the visible light is more than 50%. For this reason, effective utilization of the visible light of solar radiation, as in the photosynthesis of plants, is long “dream” of the photochemical researchers.

During the past decade, a variety of strategies have been employed to improve the visible light absorption in photocatalysis, which is related and depended on photocatalysts size, bandgap, and morphology that in turn depend on the method used for the preparation of photocatalysts.

As a narrow bandgap p-type semiconductor, copper oxide CuO has been studied like an industrially important material with low-cost production processing, nontoxic nature, abundance and good electrical and optical properties. In the last years, great efforts have been made to synthesize CuO nanostructures, due to their potential applications in a wide variety of areas including electronic and optoelectronic devices [7]. The shape of the nanostructure is equally important for controlling different properties such as optical absorption in CuO nanostructures and the catalytic activities [8].

Introduction

Generally, the synthesis of metal oxide nanoparticles is performed using different methods such as sol-gel, spray pyrolysis, hydrothermal routes, and co-precipitation method.

The main objective of this study is to synthesize pure and Sr doped CuO nanoparticles by a hydrothermal method and to highlight their structural and optical properties which are involved in the improvement of their photocatalytic activity. Their photocatalytic efficiency will be tested on the degradation of the wide used organic pollutant “methylene blue dye” under Ultraviolet radiation.

II- Overview of Photocatalytic Depollution:

II.1- Introduction:

The first studies that were reported with the concept of “heterogeneous photocatalysis” are those by Doerfler and Hauffe, published in 1964 when they carried out the oxidation of CO using zinc oxide as catalyst under illumination [9]. However, after the work by Fujishima and Honda published in 1972 [1], heterogeneous photocatalysis has become a comprehensively studied area. During the past decades, photocatalysis has been, extensively, used because of its wide range of applications in energy and environment related fields, and its great potential for solving the problems of environmental pollution and the world energy crisis.

As a green technology functioned with finely divided semiconductors (whose can accelerate a thermodynamically possible kinetically slow chemical reaction by adsorbing a photon), heterogeneous photocatalysis featured the unique advantages of operation at room temperature. Besides, such a process utilizes clean, renewable solar light as the driving force, and continues to be an important component of modern chemistry in the twenty-first century. The available existing literature in heterogeneous photocatalysis mainly focused on the advances of semiconductor TiO_2 for degradation of pollutants in water and air. However, recent researches have proven that heterogeneous photocatalysis is effective and promising for many other alternative semiconductors.

The synthetic consideration of the proper design of photocatalytic reactors and modeling of light has often been studied. These parameters were often neglected in literature but are rather important for improving efficacy and scaleup applications of photocatalytic systems.

II.2- Principles of Heterogenous Photocatalysis:

The overall process of the heterogeneous photocatalysis can be decomposed into five independent steps:

1. Transfer of the reactants in the fluid phase to the surface of catalyst
2. Adsorption of a least one of the reactants
3. A reaction in the adsorbed phase

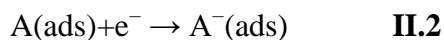
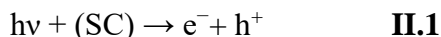
Chapter I

4. Desorption of the product(s)
5. Removal of the products from the interface region.

It has been well established that the activation mode is not concerned with Steps 1, 2, 4, and 5, although photoadsorption and photodesorption of reactants, mainly oxygen, do exist. The photocatalytic process begins when photons of energy higher or equal to the bandgap energy are absorbed by a semiconductor catalyst (SC) of the chalcogenide type (oxides (TiO₂, ZnO, ZrO₂, CeO₂...), or sulfides (CdS, ZnS...)). An electron (e⁻) from the valence band (VB) is transferred to the conduction band (CB) generating a hole (h⁺) in the VB.

The absorption of these photons creates within the bulk electron-hole pairs, which dissociate into free photoelectrons in the conduction band and photoholes in the valence band. The e⁻ and h⁺ can recombine on the surface or in the bulk of the particle releasing the energy as heat or migrate to the surface where they can react with adsorbed molecules on the surface of the particle.

In a fluid medium, the flat band potential, V_{fb}, of the semiconductor locates the energy of both charge carriers at the semiconductor–electrolyte interface and depends on the nature of the material and the system equilibrium. Adsorbed species can be reduced by CB electrons if they have redox potentials more positive than the V_{fb} of the CB and can be oxidized by holes if they have redox potentials more negative than the V_{fb} of the VB.



Each ion formed, subsequently, reacts to form the intermediates and final products. As a consequence of reactions II.(1,2 and 3), the photonic excitation of the catalyst appears as the initial step of the activation of the whole catalytic system. Thence, the efficient photon has to be considered as a reactant and the photon flux as a special fluid phase. The photon energy is adapted to the absorption of the catalyst, not to that of the reactants. The activation of the process goes through the excitation by the solid but not through that by the reactants: there is no photochemical process in the adsorbed phase but only a true heterogeneous photocatalytic regime (Fig.II.1).

Chapter I

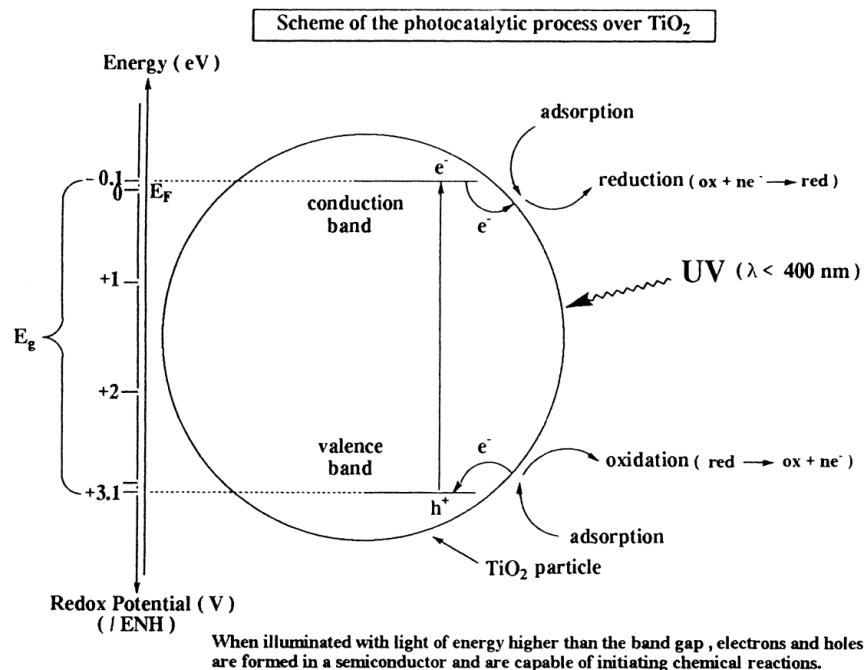


Figure II.1: Energy band diagram of a spherical Titania particle [10].

The photoefficiency can be reduced by the electron-hole recombination, which corresponds to the degradation of the photoelectric energy into heat.



where N is the neutral center and E the energy released under the form of light ($h\nu' \leq h\nu$) or of heat (Fig.II.2).

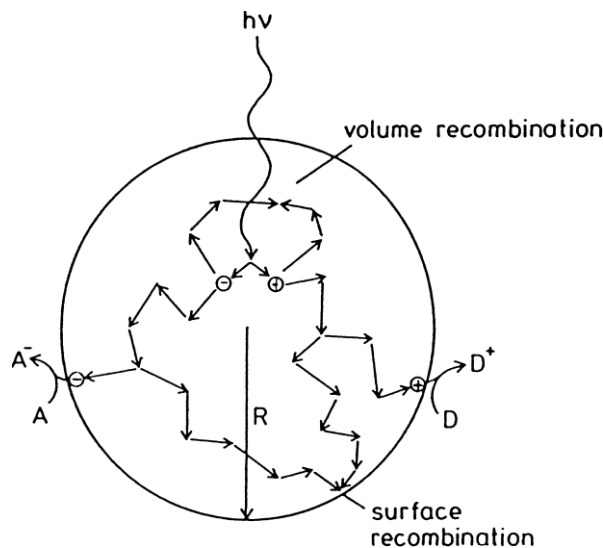


Figure II.2: Fate of electrons and holes within a spherical particle of Titania in the presence of acceptor (A) and (D) molecules [11].

Chapter I

The degradation efficiency $D(\%)$ of pollutant dye is estimated by the following formula [12]:

$$D(\%) = \frac{A_0 - A_t}{A_0} \cdot 100 \quad \text{II. 5}$$

Where: A_0 is the initial absorbance and A_t the absorbance after t exposure time.

II.3- Radiation Sources for Photocatalysis:

Due to the fact that most semiconductors photocatalysts have a bandgap in the ultraviolet (UV) region, artificial UV lamps are the most popular sources of light used in photocatalysis radiation. In this area, mercury lamps are the most commonly used, they can be divided into low-pressure mercury lamp, medium-pressure mercury lamp, and high-pressure mercury lamp [13]. Sunlight also can be used even if only 4-5% of the sunlight that reaches the earth's surface is in the 300-400 nm near UV light range. Although, solar energy has limitations due to the graphical variations when compared with artificial UV lamps. However, ongoing interests and developments in harnessing solar energy are expected to increase its use in photocatalytic degradation applications.

II.4- Factors Affecting the Degradation Performance:

II.4.1- Catalyst Loading:

It is known that the optimal concentration of the photocatalyst depends on the experimental conditions and the geometry of the photoreactor. The amount of catalyst added is directly proportional to the photocatalytic reaction rate, the concentration of the catalyst particles affects the overall photocatalysis reaction rate in a true heterogeneous catalytic regime. However, several studies have shown that when the amount of catalyst is above a certain level (saturation stage), the light photon adsorption rate decreases radially because of the appearance of a light felting effect by the catalyst particles itself [14].

II.4.2- PH of the Solution:

PH effect is one of the most impactful factors on the photocatalytic reactions and it has been extensively studied. The pH in aqueous solution enormously affects the size of aggregates as well as the charge of every different photocatalyst, whereas the point of zero charges which is the point when the surface charge is zero, varies from photocatalyst to another [15]. In figure II.3 several semiconductors and their band edge positions in contact with aqueous media at pH=0 are presented. The band levels usually shift with a change in pH (0.059 V/pH) for oxide materials.

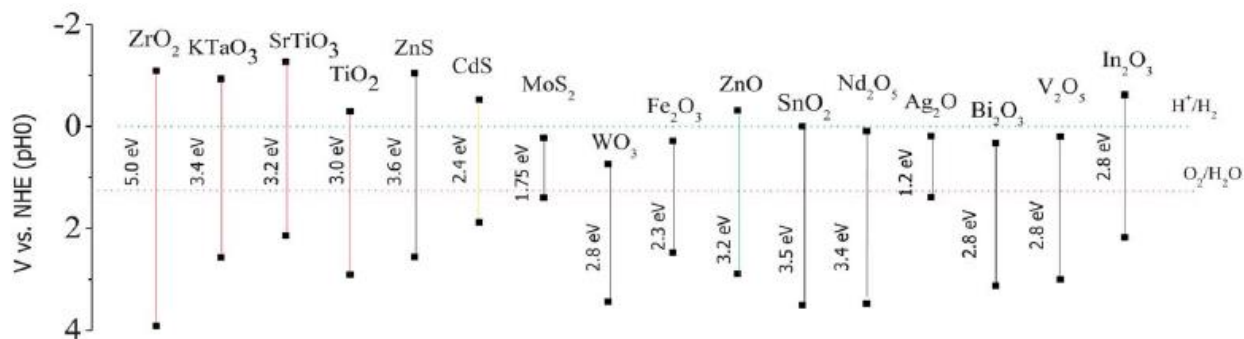


Figure II.3: Band edge positions of some semiconductors at pH=0 [16].

II.4.3- Size and Structure of the Photocatalyst:

Many studies have shown that the speed of recombination of pairs (e^-/h^+) is considerably depending on the Surface morphology, particle size and agglomerate size of the photocatalyst. Hence, the structure and size particles are important factors which affect the photocatalytic efficiency because there is a direct relationship between organic compounds and surface coverage of the photocatalyst [17]. Furthermore, it has been found that the number of photons striking the photocatalyst controls the rate of reaction which signifies that their action takes place only in the absorbed phase of the photocatalyst [18,19].

II.4.4- Temperature Effect:

The temperature plays an important role in photocatalytic reactions by modifying the mobility and the rate of recombination of the charges of the photocatalyst. Temperature, also, acts on the adsorption and desorption properties of the photocatalyst surface molecules, since adsorption of organic compounds on particles surface decreases at temperatures higher than 80°C

Chapter I

[18]. On the contrary, temperatures lower than 80°C favors the adsorption, whereas, further reduction of reaction temperature to 0°C results in an increase in the apparent activation energy [20]. Therefore, the temperature range between 20-80°C has been regarded as the desired temperature for effective photodegradation.

II.4.5- Concentration and Nature of the Pollutants:

Two other factors which they can affect the degradation rate of the dyes and hazardous chemicals are the nature of pollutants and their concentration in the reaction mixture. The photocatalytic act decreases with the increasing quantity of the pollutant as well as its nature. The high initial concentration of pollutants in water means a high concentration of adsorbed pollutants which saturates the surface and so the penetration of photons on the surface is reduced [21].

As pollutant we have chosen The Methylene Blue which is a formal derivative of phenothiazine(C₁₆H₁₈ClN₃S). It is a dark green powder that yields a blue solution in water. The hydrated form has 3 molecules of water per unit of methylene blue. Methylene blue has a pH of 6 in water(10g/l) at 25 °C (77 °F).

II.5- Photocatalytic Semiconductors Classification:

There are four typical categories of photocatalytic semiconductors [15], including:

1. Metal oxides: Simple binary oxides with a d-transition metal, the most studied metal oxides with photocatalytic purposes are (TiO₂, ZnO, WO₃, Fe₂O₃...)
2. Chalcogenides (Other than Oxides): metal sulfides are the most common semiconducting materials studied because of their narrow bandgap (CdS, ZnS, Sb₂S₃, Bi₂S₃, MoS...)
3. Ternary Compounds: Various metallates, oxysulfides, oxyhalides, and oxynitrides can be classified as photocatalytic ternary semiconductors which can be activated with visible light radiation
4. Quaternary Compounds: Oxides, oxynitrides, oxysulfides, and oxyhalides as quaternary compounds also have been investigated for evaluation of their activity in the degradation of organic pollutants and water splitting.

Chapter I

Table II.1 Common photocatalytic semiconductors, band gap energy, and the corresponding absorption edge [15].

semiconductor	Band gap (eV)	Absorption edge (nm)
Binary compounds		
Metal oxides		
Cu ₂ O	2.0–2.2	564–620
TiO ₂	3.00	413
Fe ₂ O ₃	2.30	539
ZnO	3.20	388
Chalcogenides		
ZnS	3.60	344
CdS	2.40	517
MoS ₂	1.75	709
Ternary Compounds		
FeTiO ₃	2.80	443
SrTiO ₃	3.20	388
Quaternary Compounds		
Bi ₄ NbO ₈ Cl	2.38	521
LaTiO ₂ N	2.10	590

II.6- Nanocrystalline Photocatalysts:

During the last twenty years, the interest in nano-semiconductors photocatalysts and their application in photochemistry has been grown rapidly. Several review articles have been published concerning the studies of nanoparticles, due to the fact that the materials in nano-size show the unique properties that do not appear in the micro-size. Two main reasons that make particles with diameters ranging between 1 and 100 nm different from the bulk properties are due to the surface effect and quantum size effect [22]. An important class of nanomaterials that have generated a particular interest in research during the past decade are metal oxides. Most of these compounds are gap semiconductors whose energy corresponds to the energy of UV light. Others have a gap allowing them a strong absorption in the visible range. These properties can be exploited to produce electronic systems excited by UV-Vis light. Furthermore, the electronic process that occurs after the absorption of UV-vis light can lead to different chemical reactions in the surrounding medium of semiconductor. As a result, semiconductor nanomaterials are widely applied as photo-catalyst due to their large specific surfaces and the relative ease of their introduction as purifiers in polluted environments [23].

II.7- Characteristics of Cupric Oxide:

Copper oxides exist in two different forms: cupric oxide (CuO) and cuprous oxide (Cu₂O), depending on the valence state of copper. Copper(II) oxide or cupric oxide is an inorganic black solid compound with the formula CuO (Fig.II.4). It is known in mineral form as tenorite and is a product of copper mining and the precursor to many other copper-containing products and chemical compounds.



Figure II.4: Copper Oxide CuO

This compound has attracted particular attention because it is the simplest member of the family of copper compounds and exhibits a range of potentially useful physical properties, such as high temperature superconductivity, electron correlation effects, and spin dynamics. Copper oxide is relatively cheap, easily mixed with polarized liquids (i.e., water) and polymers, and relatively stable in terms of both chemical and physical properties. Highly ionic nanoparticulate metal oxides, such as CuO, may be particularly valuable as photocatalyst and antimicrobial agents as they can be prepared with extremely high surface areas and unusual crystal morphologies.

The crystal structure of CuO is in the monoclinic space group C2/c; with four formula units per unit cell, as shown in figure II.5. The lattice constants are $a = 4.6837 \text{ \AA}$, $b = 3.4226 \text{ \AA}$, and $c = 5.1288 \text{ \AA}$, and $\beta = 99.54^\circ$ [24].

Chapter I

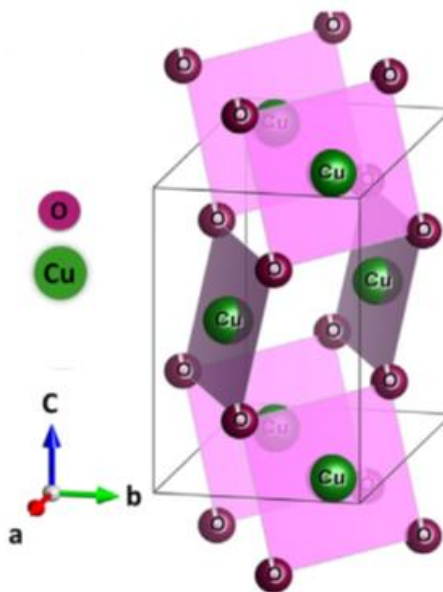


Figure II.5: Elementary CuO cell [25].

Among different semiconducting metal oxides, copper oxide (CuO) has been studied as a unique and attractive mono-oxide material for both fundamental investigations and practical applications. The CuO is an important p-type/positive-doped, transition-metal-oxide semiconductor, having a narrow bandgap with a band gap of 1.2 – 1.9 eV [26]. Not much is known about the electronic structure of CuO. Investigations of the interband absorption and hence of the bandgap energy as well as on the nature of transition, i.e., direct or indirect, are very scarce and the results do not provide an unambiguous assignment [27].

CuO semiconductors exhibit a versatile range of applications such as fabrication of electrical, optical, and photovoltaic devices; selective gas sensing devices; heterogeneous catalysts; magnetic storage media; field-emission devices (e.g., field-emission gun); solar cells; and Li-ion electrode materials. CuO also possesses complex magnetic phases and forms the basis for several high-TC superconductors (i.e., superconductors for which the Curie temperature T_C is high) and materials with high magnetoresistance.

III-Elaboration of Pure CuO and Sr Doped CuO Photocatalysts:

III.1- Introduction:

CuO nanoparticles are generally synthesized by different methods such as thermal decomposition, metal salt reduction, microemulsion, laser ablation, DC arc discharge, solvothermal and hydrothermal technique.

Hydrothermal processing is a non-conventional method to obtain nanocrystalline inorganic materials. A direct precursor-product correlation exists allowing the synthesis of almost any nanomaterials without the presence of other directing agents. The hydrothermal synthesis uses the solubility in water of almost all inorganic substances at elevated temperatures and pressures, and subsequent crystallization of the dissolved material from the fluid.

III.2- Elaboration of Pure CuO and Sr Doped CuO:

III.2.1- Elaboration of Pure CuO Nanoparticles:

To synthesis CuO nanoparticles, we have proceeded by the hydrothermal method. In a typical preparation process, 1 g of CuSO₄ copper sulfate was dissolved in 80 ml of distilled water in a glass vial and was well sonicated in a sonicator then stirred using a magnetic bar for few minutes. Subsequently 1g of NaOH soda was added to the CuSO₄ solution and sonicated and stirred again for 30 minutes. The reaction mixture was transferred into a stainless-steel Teflon lined metallic autoclave of 100 ml capacity (Fig.III.1) and sealed under ordinary conditions.

The autoclave was, then, placed inside a furnace and heated to 200°C. The solution was maintained at this temperature for 1 hour and after cooled to room temperature inside the furnace. The final product obtained was a black powder.



Fig.III.1: Hydrothermal autoclave.

III.2.2- Elaboration of Sr Doped CuO Nanoparticles:

Sr doped CuO nanoparticles were prepared in the same manner after adding a weighed mass of strontium salt SrCl₂ to the copper sulfate. Different Sr weight % were used. In table III.1 we have reported the corresponding Sr quantities used for each percentage:

Table III.1: The quantities of reactants used for each Sr percentage.

Percentage of Sr (%)	m _{CuSO4} (g)	m _{NaOH} (g)	m _{SrCl2} (g)
1%Sr	0,99	0,99	0,02
2%Sr	0,98	0,98	0,04
3%Sr	0,97	0,97	0,06
4%Sr	0,96	0,96	0,08
5%Sr	0,95	0,95	0,10
6%Sr	0,94	0,94	0,12
8%Sr	0,92	0,92	0,16
10%Sr	0,90	0,90	0,20

III.3- Washing:

After the heat treatment, a black precipitate deposit was obtained at the bottom of the autoclave. Firstly, the precipitate was isolated by pouring the solution contained in the autoclave. After that, the obtained powder was washed several times. The process was, three times, repeated using distilled water and in the fourth time using ethanol. The final step of washing process was carried in the same manner using distilled water two times successively in the aim to eliminate any trace of ethanol and residual reactants on the surface of particles powder. To extract the powders, we used each time a centrifuge of 3500 rpm during 1minute (Fig.III.2).



Figure III.2: centrifuge machine.

III.4- Drying:

Finally, the powders obtained after washing were put in glass lenses with $\phi=15$ cm diameter and heated at 80°C in a furnace for 18h. The recovered powders (Fig.III.3) were used to carry out the structural and optical characterization as well as to evaluate their photocatalytic efficiency on the degradation of organic pollutant.



Figure III.3: Recovered powders after the drying treatment.

IV- Structural and Optical Characterization of Elaborated Photocatalysts (Pure CuO and Sr Doped CuO):

IV.1- Structural Characterization:

Several techniques allow a structural study on very small materials such as nanocrystals of semiconductors. Direct observation by electron microscopy, X-ray diffraction, Raman spectroscopy, and Infra-Red spectroscopy are among the most widely used methods. These last two methods are often complementary. The first permits the study of crystalline structure and crystallographic parameters of the material; while the second allows the identification of the chemical bonds between the material atoms based on their mode of vibration.

IV.1.1- X-Ray Diffraction:

X-ray diffraction allows us to deduce the crystalline phases present in the material, to establish the symmetry and orientation of the crystals (texture), to highlight the crystal defects as well as the determination of several other parameters such as the average crystallite size, degree of crystallinity and even approach of the presence of impurities in the crystal (doping elements).

The diffractograms obtained from the samples were carried out using an X'pert PRO PANalytical type diffractometer (Fig.IV.1) and an X-ray beam of monochromatic wavelength $\lambda_{K\alpha}$ (Cu) = 1.5406Å.



Figure IV.1: Photograph of the X'pert PRO PANalytical type diffractometer.

IV.1.1.1- Identification of the formed phases:

The various powders obtained at the end of the hydro-thermal cycle were analyzed using X-ray diffraction at room temperature. The obtained spectra are shown in figure IV.2.

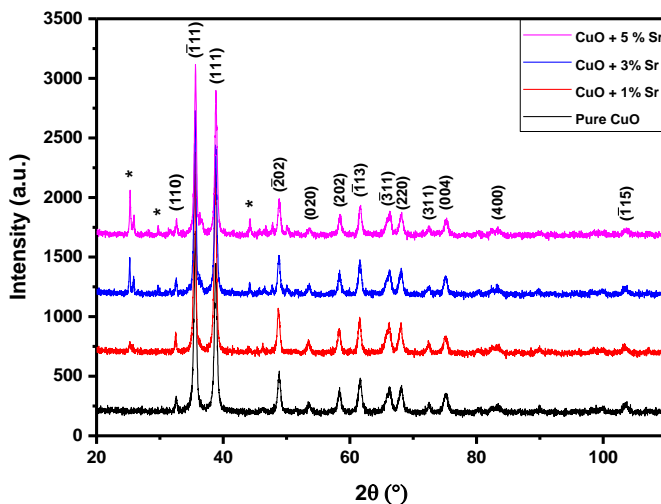


Figure IV.2: XRD spectra of different Sr doped CuO powders, * peaks of SrO secondary phase.

The spectra reveal diffraction peaks corresponding to the CuO phase listed in the JCPDS file 05-0661. This phase has a monoclinic structure belonging to the symmetry group C2/c and whose lattice parameters are as follows: $a = 4.684 \text{ \AA}$, $b = 3.425 \text{ \AA}$, $c = 5.129 \text{ \AA}$, $\beta = 99.47^\circ$. The relative intensities of the different lines calculated from these spectra, both by direct measurement of the diffraction peaks high, and by the evaluation of the peak area (assuming a Gaussian distribution) are quite close to those listed in the JCPDS file (Tab.IV.1). This fact points out, on the one hand, a good crystallinity of the powders and on the other hand the completely random orientation of the crystallites.

Table IV.1: Angle and intensity of diffraction lines of the CuO phase obtained from the pure CuO powder.

2 Θ	Plane	I/I ₀ (JCPDS 05-0661)	I/I ₀	A/A ₀
32,58	1 1 0	12	8	5
35,59	0 0 2 - $\bar{1}$ 1 1	49 - 100	100	100
38,82	1 1 1 - 2 0 0	96 - 30	82	89
46,26	$\bar{1}$ 1 2	3	2	2
48,83	$\bar{2}$ 0 2	25	21	25

53,57	0 2 0	8	4	6
58,34	2 0 2	14	11	15
61,62	$\bar{1}$ 1 3	20	18	26
66,17	$\bar{3}$ 1 1	15	12	25
68,07	2 2 0	19	13	21
72,50	3 1 1	7	4	5
75,15	0 0 4 – $\bar{2}$ 2 2	6 - 7	10	16
103,55	$\bar{1}$ 1 5	4	4	9

With I = peak's high, I_0 = high of the most intense peak, A = peak's area, A_0 = area of the most intense peak.

In the case of powders doped with Sr, the corresponding diffraction spectra reveal secondary diffraction lines whose intensity increases with the additions of Sr.

Elavarasan and Chung-Kuang Yang in a recent work on the development of CuO nanoparticles doped with strontium [28], obtained a similar X-ray diffraction spectrum (Fig.IV.3).

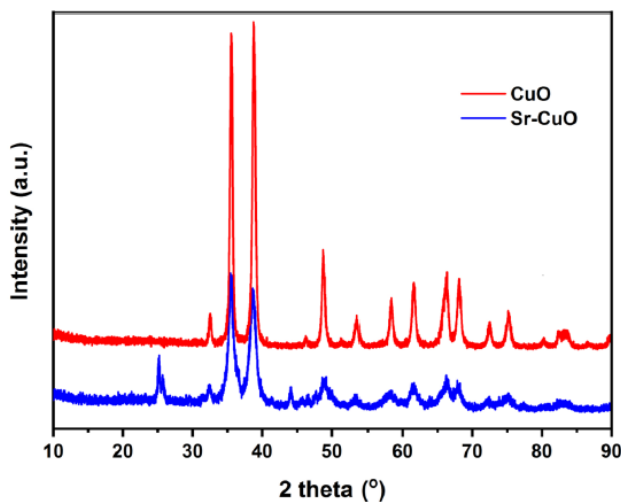


Figure IV.3: XRD spectrum of CuO and Sr-CuO obtained by Elavarasan and Chung-Kuang Yang [28].

These authors consider that the lines obtained in the case of doped CuO correspond to a single-phase (Sr-CuO) of monoclinic structure and belonging to the same symmetry group $C2/c$. They attribute the diffraction lines shift, obtained in their case, and the appearance of new lines to the distortions corroborating the introduction of the Sr cation into the Bravais lattice of the CuO

Chapter III

phase. We think, rather, that the solubility of Sr in the CuO lattice, although it exists, remains limited.

On effect, we have reported in table IV.2, the relative intensities obtained from our spectra corresponding to the Sr doped powders. We notice that these values are weakly affected by Sr additions, demonstrating that Sr only weakly affects the crystal structure of CuO. Furthermore, the shift of the lines corresponding to the CuO phase remains relatively small, so it can be deduced that the solubility of the Sr²⁺ ion in the Bravais lattice of the CuO phase is limited.

The secondary peaks which appear in our spectra are very close to those obtained by M.M. Rahman et al in their work on the development of carbon nanotube decorated with SrO nanoparticles [29]. These authors identify the formed phases using a JCPDS files 001-1113, 6-520, 75-0263 and 01-073-0661.

The limited solubility of Sr in CuO lattice is probably linked to the large difference between the Cu²⁺ cation size (73 pm) and the Sr²⁺ cation size (118 pm).

Table IV.2: Relative intensities of different diffraction peaks recorded from Sr doped CuO powders.

2θ	Plane	I/I₀ Pure CuO	I/I₀ CuO+1% Sr	I/I₀ CuO+3% Sr	I/I₀ CuO+5% Sr
32,58	1 1 0	8	9	8	9
35,59	0 0 2, $\bar{1}$ 1 1	100	100	100	100
38,82	1 1 1, 2 0 0	82	90	84	84
46,26	$\bar{1}$ 1 2	2	2	2	3
48,83	$\bar{2}$ 0 2	21	22	21	21
53,57	0 2 0	4	5	5	4
58,34	2 0 2	11	11	11	11
61,62	$\bar{1}$ 1 3	18	17	18	18
66,17	$\bar{3}$ 1 1	12	13	12	12
68,07	2 2 0	13	13	13	12
72,50	3 1 1	4	5	4	3
75,15	0 0 4, $\bar{2}$ 2 2	10	8	10	9
103,55	$\bar{1}$ 1 5	4	3	3	3

Cell parameters calculated from the obtained spectra (Fig.IV.4, Tab.3), show that these parameters do not significantly change with Sr additions, and are practically the same as those given by the JCPDS file05-0661, confirming the limited solubility of Sr²⁺ in CuO lattice.

Chapter III

It can be noticed, however, that the cell parameters are slightly weaker than those reported by the JCPDS file 05-0661 (Tab.IV.3).

This fact results in a diminution of cell volume in the case of the prepared powders. Besides, the cell parameters of CuO + 1% Sr powder are higher than the parameters of other powders.

Table IV.3: Cell parameters of pure and Sr doped CuO phases.

Powder	a(Å)	b(Å)	c(Å)	Volume (Å) ³
JCPDS 05-0661	3,425	4,684	5,129	81,16
Pure CuO	3,421	4,677	5,124	80,87
CuO + 1% Sr	3,426	4,694	5,128	81,34
CuO + 3% Sr	3,422	4,675	5,127	80,90
CuO + 5% Sr	3,419	4,663	5,122	80,55

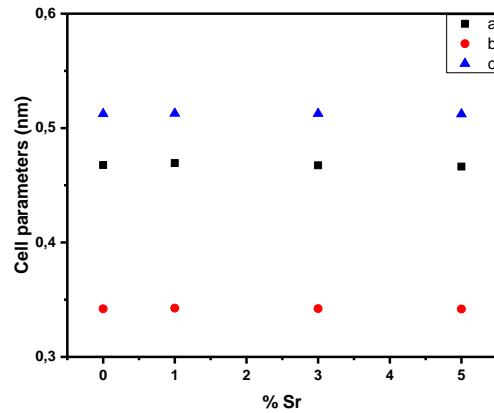


Figure IV.4: CuO phase cell parameters as a function of the Sr wt %.

We used the method proposed by Wilson to approximate the deformations induced by the insertion of the Sr²⁺ cation in the CuO lattice in the three main crystallographic directions [hkl] using the following expression:

$$\varepsilon^m_{(hkl)} = \left(\frac{\Delta d_{(hkl)}}{d_{0(hkl)}} \right) \quad \text{IV. 1}$$

The $d_{0(hkl)}$, represents the reticular distance of the planes (hkl) in a crystal without deformation (we have considered the parameters of the crystal listed in the JCPDS file05-0661 and $\Delta d_{hkl} = d_{(hkl)} - d_{0(hkl)}$).

In Table IV.4, we have reported the calculated values of the $\epsilon^m_{[hkl]}$ parameter according to the three main directions.

Table IV.4: Values of the deformations in the CuO lattice in the three main crystallographic directions.

Type of powder	$\epsilon^m_{[100]}$	$\epsilon^m_{[010]}$	$\epsilon^m_{[001]}$
Pure CuO	0,0030	-0,0381	-0,0029
CuO+ 1% Sr	0,0048	-0,0366	-0,0008
CuO+ 3% Sr	0,0034	-0,0376	-0,0024
CuO +5% Sr	0,0020	-0,0386	-0,0038

We note, from these results, an expansion of the crystallites in the [100] direction and conversely a compression in the [010] and [001] directions. Moreover, the results show a remarkable fact; i.e. the evolution of deformations (in absolute value) in the direction [100] evolves oppositely to those of the other two directions. In other word the deformation in the direction [100] increases, in absolute value, when the other two decrease and vice versa.

IV.1.1.2- Crystallites size:

The technique of X-ray diffraction by nanometric powders is widely used to approximate the average size of the particles in the perpendicular direction to the diffraction planes. The mostly used method, is based on Scherrer's formula:

$$D = \frac{K\lambda}{\beta \cos\theta} \quad \text{IV. 2}$$

Where D represents the average size of the particles in the perpendicular direction to the diffraction planes; $\lambda_{k\alpha Cu} = 0.15406$ nm is the wavelength of the X-ray used and θ ; the diffraction angle corresponding to the peak. K is Scherer's constant; it is usually taken equal to 0.9 when β is taken equal to the width at mid-height of the diffraction peak (FWHM). In the general case, K depends on the size distribution of the particles [30], for example Pielaszek founds that the most appropriate

value of K in the case of a sample consisting of particles of widely dispersed sizes was equal to 0.5 [31].

Using equation 2 we calculated the particles size along the perpendicular directions to the (200), (020) and (002) planes, i.e. along the three main crystallographic axes. The values calculated for the different weight Sr percentages are reported in table IV.5 We have also reported, in the same table, the average number of primitive cells in each direction using the expression:

$$n_{(hkl)} = \frac{D_{hkl}}{a_{(hkl)}} \quad \text{IV. 3}$$

Table IV.5: Particle Size corresponding to different crystallographic directions.

Powder	D _[200] (nm)	n[200]	D _[020] (nm)	n[020]	D _[002] (nm)	n[002]
Pure CuO	16,19	47,3	12,82	27,4	17,33	33,8
CuO + 1% Sr	17,43	50,9	13,87	29,6	20,56	40,1
CuO + 3% Sr	17,58	51,4	15,76	33,7	22,25	43,4
CuO + 5% Sr	17,54	51,3	12,26	26,3	21,06	41,1

These results show that the particle size along the three crystallographic axes is not the same. Thus, we have D [002]> D [200]> D [020] which demonstrates that the CuO crystallites formed during the elaboration process are more elongated in the [001] direction. This result is probably related to the structure of CuO itself, which contains elongated octahedra of O²⁻ anions with a Cu²⁺ cation in the center. The four short Cu-O bonds form parallelograms which are slightly distorted rectangles [32]. These rectangles bond together to form roughly wavy sheets parallel to the planes (101). We notice, moreover, that the weak additions of Sr (1%) induce a notable growth of crystallites according to directions [100] and [001] while the growth of crystallites according to direction [010] remains moderate. The number of cells by the principal direction also shows that the growth of crystallites is more consistent in the two directions [100] and [001] than in the direction [010].

Furthermore, we deduce from expression IV.2 that:

$$\beta = \frac{K\lambda}{D \cos \theta} \quad \text{IV. 4}$$

This equation expresses a linear relation between β and $1/\cos(\theta)$. The slope of the line representing such a relationship is simply equal to $K\lambda/D$ which, in theory, makes it possible to calculate the average size of the particles. In order to check the validity of the relation 2, we have represented, in figure IV.5, the variation of β as a function of $(1/\cos(\theta))$ in the case of pure CuO powder. We

note, indeed, that the obtained curve is linear, however, its extrapolation at the origin does not cancel out as equation IV.4 suggests.

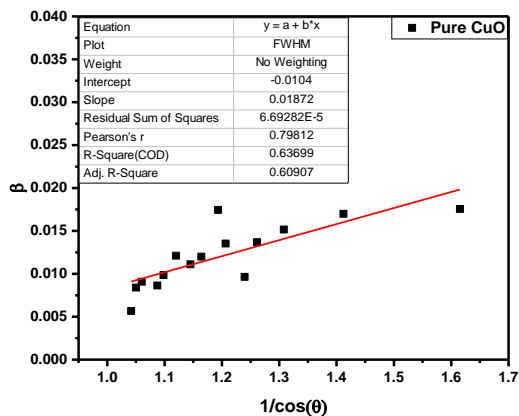


Figure IV.5: variation of β as a function of $1/\cos(\theta)$.

Such a result reflects the fact that the width of the diffraction peaks is not linked, only, to the size of the particles but also to other factors; mainly, the residual stresses within the different particles (as a result of the particle development process) and especially the diffraction device itself. This last factor should normally be approximated using a reference sample (generally by using a pure silicon powder) which would be mixed with the analyzed powder, the broadening of the peaks of the reference powder corresponds to experimental width. Unfortunately, we do not have any possibility to perform such tests.

If we assume that the distribution of the intensity of the diffraction peaks is Laurentian (Gauchy), we will have in this case: $\beta = \beta_{\phi} + \beta_s$, with β_{ϕ} the width of the peak due to the finite size of the particles and β_s the width induced residual stresses [33]. We therefore deduce that the size of the crystallites calculated directly by expression 4 and reported in table IV.6 are values below the actual values.

Table IV.6: Average particle size (nm)

samples	Average particle Size (nm)
Pure CuO	7,41
CuO +1% Sr	8,80
CuO +3% Sr	6,46
CuO+5% Sr	5,05

If, on the contrary, we suppose that the diffraction line has a Gaussian shape both because of the finite size of the crystallites and experimental device itself (opening of the slit, etc.), we can write in this case:

$$\beta^2 = \beta_\phi^2 + \beta_s^2$$

β being the width at mid-height measured, β_ϕ the width related to the size of the crystallites and β_s width induced by the residual stresses. We conclude, therefore, that $\beta_\phi = \sqrt{\beta^2 - \beta_s^2}$ with, of course $\beta_\phi = \frac{k\lambda}{D \cos \theta}$.

IV.1.1.3- Williamson-Hall deconvolution method:

Considering that the spatial distribution of the diffracted X-Ray beam follows a Lorentz distribution, we can write the width of peak $\beta = \beta_\phi + \beta_s$, where β_ϕ represents the width at mid-height corrected for the effects of the experimental width and β_s the width induced by the residual stresses.

We can easily find a relation between the width at half height and the stresses from Bragg's law. We have, in fact, from this relationship: $2d_{hkl} \sin \theta = n\lambda$

By taking the differential of this expression, we will have $\frac{\Delta d_{hkl}}{d_{hkl}} \sin \theta = -\cos \theta \cdot \Delta \theta$. We deduce,

by taking $\Delta \theta = \beta_s$ and $\frac{\Delta d_{hkl}}{d_{hkl}} = \epsilon$, that $\beta_s = -\epsilon \operatorname{tg} \theta$. In the case of powder compression, as is

the case in the hydrothermal procedure ϵ actually has a negative value, but its physical meaning is rather related to its absolute value. We can therefore simply write: $\beta_s = \epsilon \operatorname{tg} \theta$

In their original article, Williamson and Hall instead give the following relationship [34]:

$$\beta_s = 2\epsilon \operatorname{tg} \theta$$

Several authors [35,36] use a factor of 4 instead of 2 in the previous relation which gives values of ϵ four times smaller.

By replacing β_ϕ and β_s by their respective expressions we obtain:

$$\beta = \beta_\phi + \beta_s = \frac{k\lambda}{D \cos \theta} + 4\epsilon \operatorname{tg} \theta$$

This expression that can be easily transformed into the following form:

$$\beta \cdot \cos \theta = \frac{k\lambda}{D} + 4\epsilon \sin \theta \quad \text{IV. 5}$$

This relation shows that $\beta \cdot \cos\theta$ varies linearly with $4 \cdot \sin\theta$, the slope of the representative curve makes it possible to calculate the residual deformation ϵ . The intersection of the line with the axis, $\beta \cos\theta$, makes it possible to determine the average size of the nanoparticles.

In the figures IV.6 we have represented the curves obtained by this method in the case of the four prepared powders.

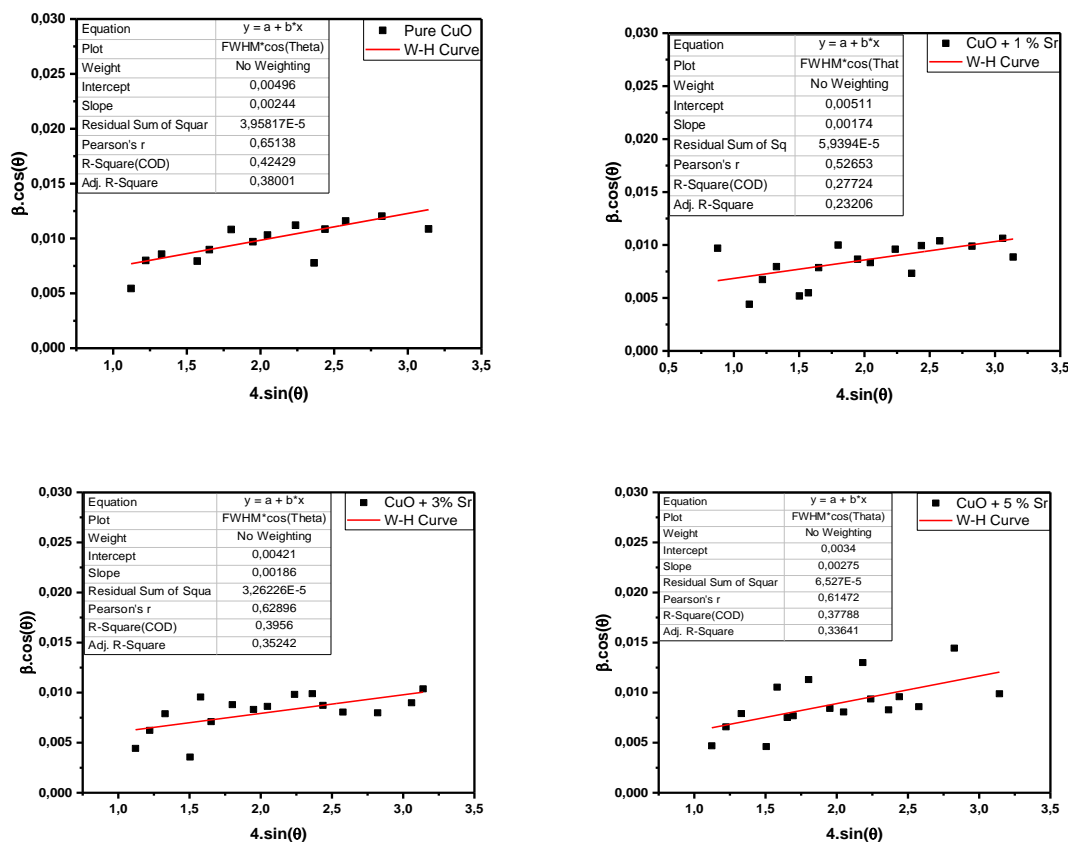


Figure IV.6: Representation of Williamson-Hall deconvolution curve for the pure CuO and Sr doped CuO powders.

The average sizes as well as the residual deformations corresponding to the different powders and calculated by this method are reported in Table IV.7.

Table IV.7: Particles size and stress calculated by Williamson-Hall method.

Powder	Particles Size (nm)	Stress
Pure CuO	27,95	0,0024
CuO+1%Sr	27,13	0,0017
CuO+3%Sr	32,93	0,0019
CuO+5%Sr	40,78	0,0028

The average particle sizes obtained are larger than those obtained using equation 2 because the peak broadening linked to the size of the crystallites is in this case smaller. We notice, moreover, that the size of the particles increases, generally, with the added content of Sr.

The residual strains approximated by this method are of the order of 0.2%. The values of these deformations vary, slightly, with the percentage of Sr additions, which shows that the percentage of Sr^{2+} cations which substitute the Cu^{2+} cations in the CuO lattice does not vary appreciably with the added percentages of Sr.

We notice that the values of the particle sizes calculated by the W-H method are relatively larger than those calculated by the Scherrer method (Fig.IV.7). This result is quite logical since in Scherrer method we neglect the widening of the diffraction peaks induced by the residual deformations. This results in an overestimation of the size effect on peak width and consequently smaller sizes are obtained. Note, in addition, that for both methods, the calculated particle size increases, generally, as a function of the additions in Sr.

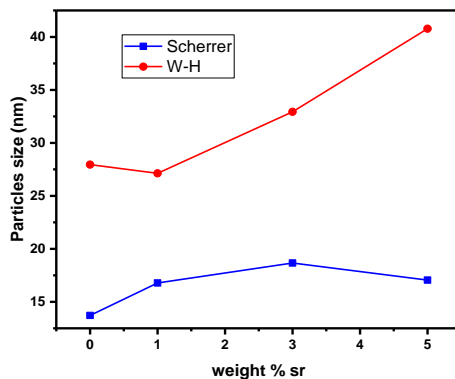


Figure IV.7: Particle sizes as a function of Sr%.

IV.1.1.4- Dislocations density in the produced CuO powders:

Dislocations are linear crystallographic defects that appear in all crystalline materials regardless of the methods of their manufacture. The presence of dislocations and their density clearly influence the properties of these materials. Theoretically, a crystalline solid is a periodic repetition, in three-dimensional space, of an atom or a group of atoms. The positions of atoms or molecules within this structure are reproduced at distances defined by lattice parameters. In reality, this repetition is not as perfect, firstly, because of the finite size of the crystals and secondly, because of the appearance of point defects (vacant, insertion), linear (dislocation) or even planar

(twin). The dislocations can move inside the crystal when it is subjected to external stresses and are the cause, therefore, of the residual deformations which appear in this material. The dislocations movement is, however, inhibited by other crystal defects as well as the presence of other dislocations within the same crystal. Thus, greater dislocation density implies greater toughness of the sample and higher hardness. It is, generally, accepted in the case of massive materials that the mechanic resistance of the materials increases with the decrease in the grains size, since the grain boundaries are major obstacles to the movements of the dislocations.

We can, therefore, think that the presence of dislocations in nanoparticles has a great importance on the properties of these physical entities.

The dislocation density δ (i.e. their total length per volume unit) in nanomaterials can be approximated using the X-ray diffraction technique with the expression proposed by Williamson and Smallman [37]:

$$\delta = \frac{3n}{D^2} \quad \text{IV. 6}$$

With D the average particle size. and n an integer, the value of $n = 1$ corresponds to the minimum of the dislocation density. The values of the dislocation densities calculated using this expression, considering the particle sizes obtained by the two preceding methods, are reported in table IV.8. These values are very close to those obtained by Saleem et al in the case of thin ZnO layers deposited by sol-gel [38].

TableIV.8: Estimation of the dislocation density.

Powder	D(Scherrer)	$\delta(10^{15}m^{-2})$	D(W-H)	$\delta(10^{15}m^{-2})$
Pure CuO	13,71	15,96	27,95	3,84
CuO 1% Sr	16,78	10,65	27,13	4,08
CuO 3% Sr	18,66	8,62	32,93	2,77
CuO 5% Sr	17,05	10,32	40,78	1,80

In their original work, Williamson and Smallman find values of δ which vary between $2 \cdot 10^{11}$ (m^{-2}) in tempered aluminum metal and $3 \cdot 10^{12}$ (m^{-2}) in tempered molybdenum and tungsten. In the case of cold-worked metals, these same authors find values that vary between $5 \cdot 10^{13}$ and $2,7 \cdot 10^{14}$ (m^{-2}) for aluminum. It can, therefore, be concluded that our powders contain a high density of dislocations, which suggests a high reactivity of these powders.

IV.1.1.5- Specific surface of the nanoparticles:

The specific surface is also an important property of nanoparticles, it measures the total surface area of the particles per weight unit. It is an important specific parameter to modulate different properties of a material. It is of particular importance in the phenomena of adsorption, heterogeneous catalysis and photocatalysis as well as in the various reactions occurring at the surfaces of nanoparticles. The specific surface area of nanoparticles can be approximated using the following expression:

$$S = \frac{6 \cdot 10^3}{D \cdot \rho} \quad \text{IV. 7}$$

used by several authors [36] and which is actually established in the case of spherical particles (see Annex 1), where S represents the specific surface in m²/g, D; the size of the particle in (nm) and ρ; the density in g / cm³. In the case of CuO, we have ρ = 6.31 g / cm³.

Otherwise Hoon et al [39] propose the following expression to calculate the specific surface area of nanoparticles of quadratic structure:

$$S = \frac{2D_a + 4D_c}{\rho D_a \cdot D_c} \quad \text{IV. 8}$$

This expression is established, in fact, in the case of cylindrical particles (see Annex 1). Assuming that this expression remains valid in the case of our particles, taking D₁₀₀~ D₀₁₀.

Furthermore, the following formula (see Annex I) was used to estimate the specific surface in the case of prismatic particles checking the symmetry of the elementary cell:

$$S = \frac{2}{\rho} \left(\frac{1}{D_a \sin \beta} + \frac{1}{D_c \sin \beta} + \frac{1}{D_b} \right) \quad \text{IV. 9}$$

With β=81.57°.

The values of the surface calculated using the three expressions are reported in table IV.9.

Table IV.9: Specific surface areas calculated from the elaborated CuO nanoparticles.

Powder	Specific surface area (m ² /g) (spherical particles)	Specific surface area (m ² /g) (cylindrical particles)	Specific surface area (m ² /g) (prismatic particles)
Pure CuO	69,36	61,98	63,07
CuO+ 1% Sr	56,67	55,92	56,90
CuO+ 3% Sr	50,96	52,27	52,80
CuO+5% Sr	55,77	57,59	59,45

We can note that the values calculated using these three expressions are very close and they represent a large specific surface area. For example, the specific surface area calculated using expression 7 is equal to the area of a room of 7×10 (m^2). This is another factor that suggests the high reactivity of the elaborated CuO powders.

IV.1.2- Infrared Spectroscopy:

IV.1.2.1- Introduction:

Fourier Transform Infrared Spectroscopy (or FTIR: Fourier Transformed Infrared spectroscopy) is a method of structural analysis, sensitive to the nature of the bond between the atoms of a molecule. It is based on the absorption of infrared radiation by the analyzed material. By detecting the characteristic vibrations of chemical bonds, it makes it possible to analyze the chemical functions present in the material.

FTIR spectra were performed using an infrared spectrophotometer of the type: JASCO FT / IR - 6300 (Fig.IV.8) in the spectral range $400\text{-}700 \text{ cm}^{-1}$ which corresponds to the molecular vibration's domain of metal oxide compounds such as the CuO semiconductor.

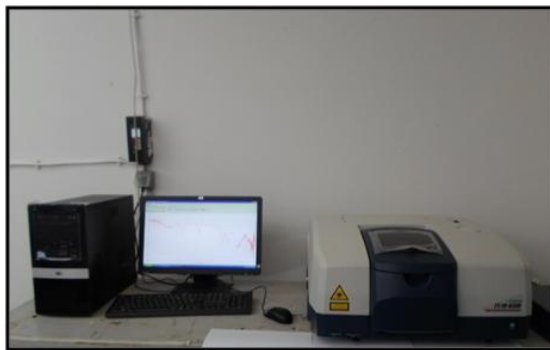


Figure IV.8: Spectrophotometer of type JASCO 6300.

IV.1.2.2- Infrared Analysis:

It has been already mentioned, Copper oxide (CuO) crystallizes in the monoclinic space group $C2/c$ with two CuO molecules per unit cell. The positions of atoms in the elementary cell are respectively:

Cu:1: $(1/4, 1/4, 0)$; Cu:2: $(3/4, 1/4, 1/2)$; O:3: $(0, \beta, 1/2)$; O:4: $(0, -\beta, 3/4)$, with $\beta = 0,4184$.

Copper forms four coplanar bonds with oxygen, which, in turn, is coordinated by four copper atoms in a tetrahedral space. In three-dimensional space, the lattice of CuO crystal structure can be constructed from two sets of planar chains $[\text{CuO}_2]$ directed along $[110]$ and $[\bar{1}\bar{1}0]$ directions and alternately stacked along the $[001]$ direction (Fig.IV.9).

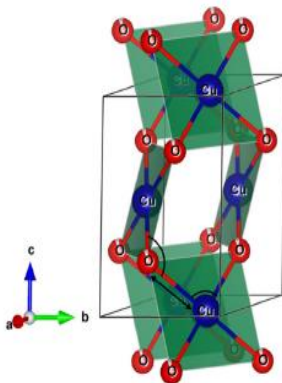


Figure IV.9: The elementary cell of the CuO phase showing that this structure is obtained by successive stacking of (CuO_2) Chains [40].

The lattice factor Γ obtained by Kliche and Popovic based on the symmetry group theory and using data from Rousseau's tables [41] is for copper cations and oxygen anions respectively:

$$\Gamma(\text{Cu}) = 3A_u + 3B_u$$

$$\Gamma(\text{O}) = A_g + 2B_g + A_u + 2B_u$$

which gives a total factor of:

$$\Gamma(\text{CuO}) = A_g + 2B_g + 4A_u + 5B_u$$

Among these vibration modes there are three acoustic modes ($1A_u$ and $2B_u$) and will not be detected by infrared radiation. The factor $\Gamma(\text{CuO})$ therefore becomes:

$$\Gamma(\text{CuO}) = A_g + 2B_g + 3A_u + 3B_u$$

The first three modes (A_g and $2B_g$) are Raman modes and the other six ($3A_u$ and $3B_u$) are infrared modes. An infrared spectrum can therefore reveal at most the six modes of vibration mentioned above. However, in our case the infrared range studied extends from 500 to 4000 cm^{-1} , it follows that only the modes of vibration with wave numbers greater than 500 cm^{-1} will be detectable.

Spectra recorded from our powders using Fourier Transform Infrared Spectroscopy (FTIR) (Fig.IV.10) show several bands of vibration.

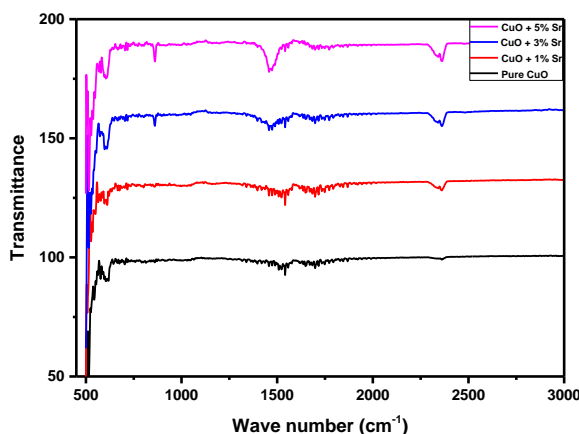


Figure IV.10: FTIR spectra of different Sr doped CuO powders.

In the case of pure CuO powder, vibration bands are observed at 510, 608, and 1540 cm^{-1} . In the case of doped powders, we notice the appearance of three other vibration bands at 850, 1466 and 2360 cm^{-1} . Note that the amplitude of the bands located at 510 and 608 cm^{-1} respectively is slightly affected by the Sr additions, which demonstrates that they are related to the vibrations of the Cu-O bond. At the opposite, the amplitude of the bands obtained at 850, 1460 and 2360 cm^{-1} respectively is the more important that when the percentage of Sr is greater.

Based on the theoretical data, above mentioned, it can be predicted that only the absorption bands located at 510 and 608 cm^{-1} would correspond to vibration modes of the CuO lattice.

In their original work on the infrared vibration modes of massive CuO in infrared, Kliche and Popovic [41] on the one hand and Hagemam et al [42] on the other hand, find vibration modes at 530 and 590 cm^{-1} . Based on theoretical bond strength calculations, Kliche concluded that the vibration mode at 530 cm^{-1} corresponds to the B_u^2 mode reflecting the stretching of the Cu-O bond along the direction [101]. The absorption band located at 590 cm^{-1} is related to the B_u^3 vibration mode, translating the stretch along the direction $[\bar{1}10]$.

In a recent work on the manufacture of CuO nano-powders by biogenic synthesis, Singh et al [43], confirm the existence of the absorption band at 530 cm^{-1} . The infrared spectra unregistered by these authors, however, revealed another mode of vibration at 1088 cm^{-1} that the authors attribute (without specifying the nature of the mode) also to the vibrations of CuO. For their part, Dar et al, in a work on the synthesis of CuO nanoparticles by the hydrothermal method [44], found vibration modes at 528 and 606 cm^{-1} which they attribute to stretching vibrations along $[\bar{2}02]$ direction. Siddiqui et al, in their investigation of nanoparticles synthesized by the hydrothermal

technique, found absorption bands at 520.4 and 604.5 cm^{-1} . The spectra realized by these authors also show a band at 2352.5 cm^{-1} , therefore very close to that which we recorded (2360 cm^{-1}). They attribute this band to the vibrations of CO_2 molecules present in air. Other authors find the bands corresponding to the vibration modes Bu^2 and Bu^3 at lower wavenumber values; 508 and 601 cm^{-1} respectively for Asha et al [45], and 510 cm^{-1} [46].

We can therefore conclude that the absorption bands obtained in our case at 510 and 608 cm^{-1} certainly correspond to the vibration modes Bu^2 and Bu^3 respectively. The relative displacement of these two absorption bands can be related to several factors, including residual strains and dislocations present in nanoparticles and also to the morphology and size of CuO nanoparticles.

The absorption band located around 860 cm^{-1} that appears in nanoparticles doped at more than 3% Sr is linked to the stretching vibration mode of the Sr-O bond [47]. It should also be noted that SrO also has a vibration mode around 605 cm^{-1} which is very close to Bu^3 mode of CuO, this explains the increase in the amplitude of this absorption band with the addition of Sr.

The absorption bands obtained at 1466, 1540 and 1700 cm^{-1} are probably related to modes of vibration of secondary products.

The results of this infrared spectroscopy study confirm the formation of nanoparticles of the CuO and CuO + SrO type in Sr doped powders synthesized by hydrothermal method.

IV.2- Optical characterization (UV-Visible Absorption):

Optical investigations are divided into two areas, absorption and emission of electromagnetic radiation by the studied materials. In our work, we have studied absorption in the UV-Visible range.

The use of UV-Visible absorption spectra allows the access to several intrinsic (optical absorption, optical gap, refractive index) and extrinsic characteristics of the produced powders (pure CuO and Sr doped CuO).

IV.2.1-UV-Visible absorption spectra analysis:

The UV-visible spectra were recorded using a Shimadzu 3100 spectrophotometer (Fig.IV.11). In figure IV.12, are reported spectra from various CuO powders homogeneously dispersed in distilled water, in the range 300-900 nm.



Figure IV.11: Shimadzu 3100 spectrophotometer.

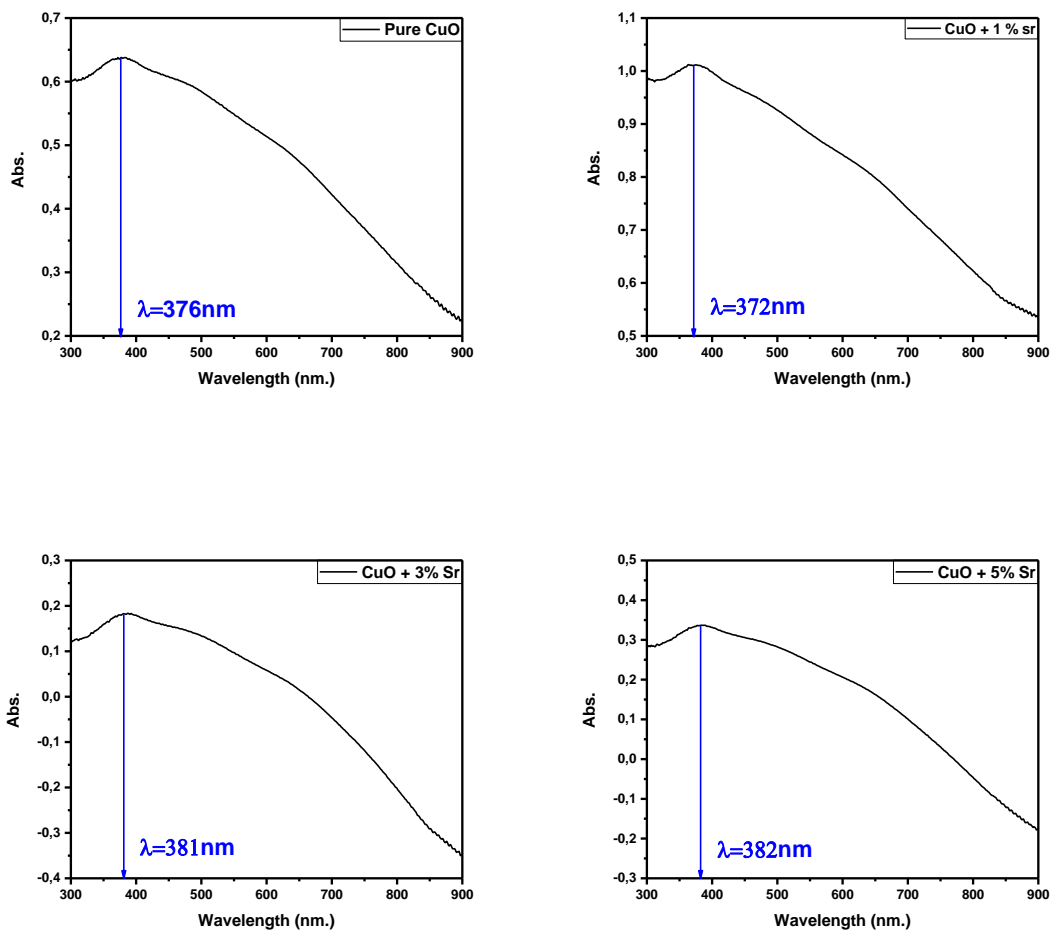


Figure IV.12: UV-Visible spectra of pure CuO and Sr doped CuO powders.

These spectra point out a maximum of absorption between 372 and 382 nm which correspond to 3,33 and 3,25 eV linked to the band edge absorption. In their study on CuO nanowires Zhao et

al [48] found values between 340 and 390 nm which agree with our values. Beyond this domain, the absorbance of powders decreases with wavelength.

The absorbance spectra realized from doped powders show the same evolution as for the pure CuO powder. We note, thus, that band edge absorption is slightly affected by Sr addition. This fact confirms, once again, that Sr solubility in CuO lattice is limited.

IV.2.2-Band Gap energy:

Based on the theory of time-dependent disturbances, one can calculate the probability that an electron has to pass from the valence band to the conduction band when it is excited by an electromagnetic wave of energy $E = h\nu$. This theory [49] shows that in the case of intrinsic semiconductors, the absorption coefficient, which represents the ratio between the transmitted intensity and the incident intensity per length unit, is related to the gap E_g by Tauc and Davis-Mott relation:

$$\alpha h\nu = B(h\nu - E_g)^{\frac{n}{2}} \quad \text{IV. 10}$$

Where B is a constant.

The exponent n depends on the type of transitions between the valence band and the conduction band; it is equal to 1 for a direct gap, 4 for an indirect gap and 3 for a forbidden transition [50]. The value of the gap is determined by the intersection of the extrapolation line of the spectrum $(\alpha h\nu)^{\frac{2}{n}} = f(h\nu)$ with the energy axis.

In UV-Vis spectroscopy, the obtained data are wavelength and absorbance, therefore the wavelength must be converted to energy, and the absorption coefficient α must be calculated from the absorbance data.

For the energy calculation we simply used Max Plank equation:

$$E = h\nu$$

Where h is the Plank constant $h=6,62.10^{-34}\text{J.s}$, and ν is the frequency of the incident photon.

$$\nu = \frac{c}{\lambda}$$

c is the light speed, $c=3*10^8\text{m/s}$.

hence, we can write:

$$E = \frac{hc}{\lambda}$$

$$E = \frac{6,62 \cdot 10^{-34}(\text{J} \cdot \text{S}) \cdot 3 \cdot 10^8(\text{m} \cdot \text{s}^{-1})}{\lambda(\text{m})}$$

$$E(\text{eV}) = \frac{1,986 \cdot 10^{-25}}{1,6 \cdot 10^{-19} \cdot \lambda}$$

$$E(\text{eV}) = \frac{12,40 \cdot 10^{-7}(\text{eV} \cdot \text{m})}{\lambda(\text{m})}$$

$$E(\text{eV}) = \frac{1240}{\lambda(\text{nm})} \quad \text{IV.11}$$

using equation IV.11, we are able to calculate directly the energy from wavelength.

In Tauc plot method, the values of the Y-axis take the values of $(\alpha h\nu)^{2/n}$, where $h\nu$ is the incident photonic energy and α is the absorbance coefficient.

α can be calculated from absorbance data using Beer-lambert's law:

$$I = I_0 e^{-\alpha l}$$

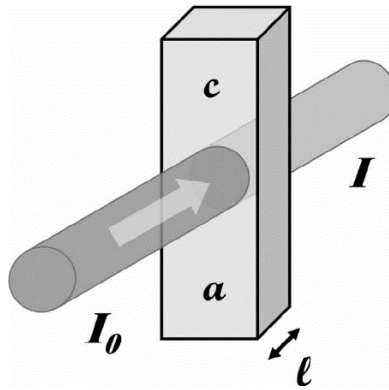


Figure IV.13: the “cuvette” model, which forms the basis of the Beer-lambert law.

In figure IV.13, I is the intensity of the transmitted light; I_0 is the intensity of the incident light; α is the absorbance coefficient; l is the path-length where the absorbance takes place.

Beer-lambert 's equation can be modified as:

$$\frac{I}{I_0} = e^{-\alpha l}$$

Taking \log_{10} of both sides:

$$\log\left(\frac{I}{I_0}\right) = \log(e^{-\alpha l})$$

$$\log\left(\frac{I}{I_0}\right) = -\alpha l \cdot \log(e)$$

$$\log\left(\frac{I_0}{I}\right) = \alpha l \cdot \log(e)$$

As absorbance is:

$$A = \log\left(\frac{I_0}{I}\right)$$

We can write:

$$A = \alpha l \cdot \log(e)$$

$$\alpha = \frac{A}{l \cdot \log(e)}$$

Replacing $\log(e)$ by its value in the last equation:

$$\alpha = 2,303 \cdot \frac{A}{l}$$

In standard cuvette, the path-length is usually equal to 10 mm, i.e.:

$$l = 10\text{mm} = 1\text{cm}$$

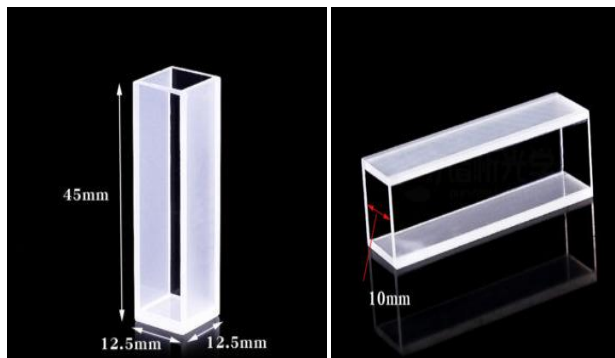


Figure IV.14: spectrometry standard cuvette.

Therefore, the equation becomes:

$$\alpha = 2,303 \cdot \frac{A}{1\text{cm}}$$

$$\alpha = 2,303 \cdot A \text{ (cm}^{-1}\text{)} \text{IV.12}$$

The unit of absorbance coefficient α would be cm^{-1} , because 2,303 is a constant and A is a dimensionless quantity. The combination between energy and equation IV.12 allows the calculation of $(\alpha h\nu)^{\frac{2}{n}}$ values in the Tauc plot method:

$$(\alpha h\nu)^{\frac{2}{n}} = (2,303.A.E)^{\frac{2}{n}}$$

In figures IV.15 we have reported the curves obtained by this method in the case of pure CuO and doped CuO powders by considering a direct gap. Extrapolation of the linear part of these spectra intersects the energy axis at the value corresponding to the gap.

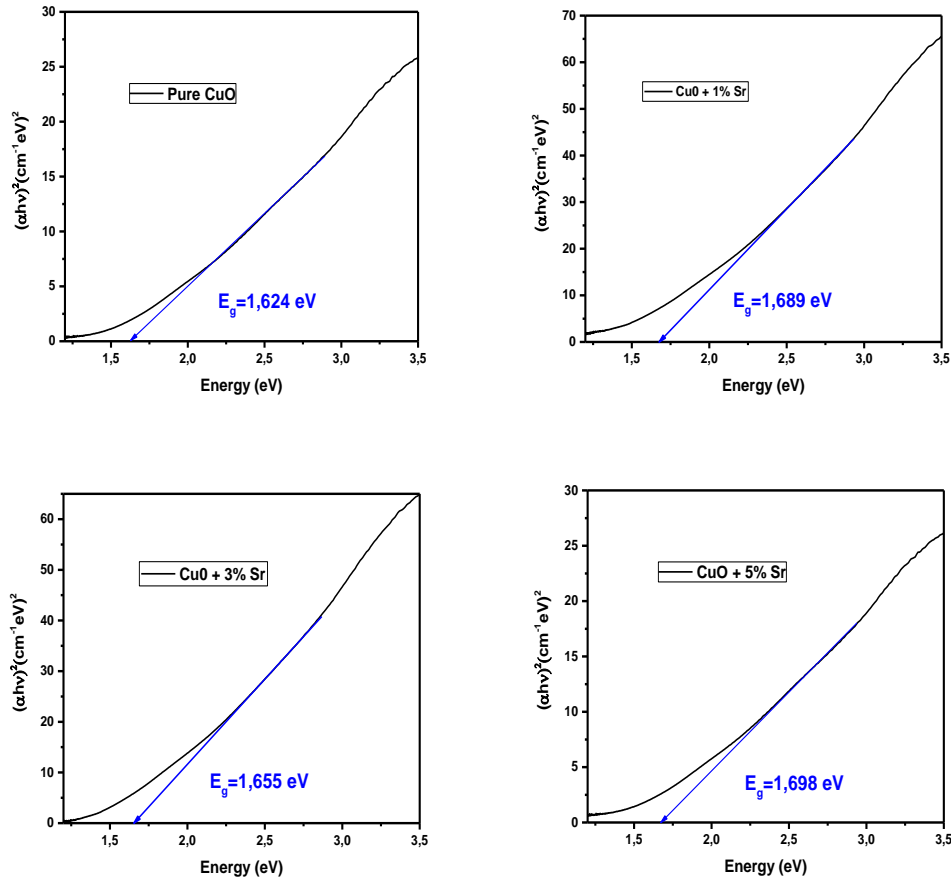


Figure IV.15: Band Gap energy estimated using Tauc method for pure and doped CuO powders.

The gap values calculated by this method (Tab.IV.10) lied between $E_g = 1,624$ eV for the pure CuO powder and $E_g = 1,698$ eV for the 5% Sr doped CuO powder. These values are very close to those found by Wang et al. (1.8 eV) [51], and Prabu et al. (1,63 eV) [52].

Table.IV.10: Gap values of pure CuO and Sr doped CuO powders.

Powders	Gap Energy (eV)
Pure CuO	1,624
CuO + 1% Sr	1,689
CuO + 3% Sr	1,655
CuO + 5% Sr	1,698

In conclusion, the gap is blue-shifted compared to the gap of the bulk CuO material (1,35 eV) [53]. This shift is linked to the well-known quantum confinement effect. It is however quite different from that calculated by the same method for CuO nanowires by Zhao et al. [48], who found 1,22 eV.

V- Evaluation of Photocatalytic Activity of Elaborated Photocatalysts (Pure CuO and Sr Doped CuO):

The photocatalytic activity of the prepared CuO nano-powders was approached by studying the degradation of methylene blue dye (MB) dissolved in distilled water. For this study, 1 ml of MB solution (1% Mol) was mixed with 99 ml of water, then 25 ml of the obtained solution were again mixed with 475 ml of water so that the solution has a MB concentration equal to 5.10^{-6} Mol. After that 0.4g of CuO powder (doped or non-doped) were added to 50 ml of this last solution and exposed for 5 min to ultrasounds. At the end of this step, the solution changes the color from blue to dark (Fig.V.1).



Figure 1: MB solution with CuO NPs before and after exposition to Ultrasounds.

V.1- Study of methylene blue photolysis:

We started this study by pure MB solution photolysis (without the addition of CuO nanoparticles). The MB solution was exposed to UV radiation ($\lambda = 365$ nm) for a total period equal to 40 min. After each interval of 10 min, 5 ml of the solution were withdrawn and an absorbance spectrum was recorded. The absorbance spectra obtained are shown in Figure V.2. These spectra demonstrate the two absorption bands of MB with maximum at 614 and 664 nm. It is also noted that exposure of the MB solution to ultra-violet radiation has no significant effect and the degradation of MB is less than 5.5% (Fig.V.3). The stability of solution was reached after around 30 min of exposure.

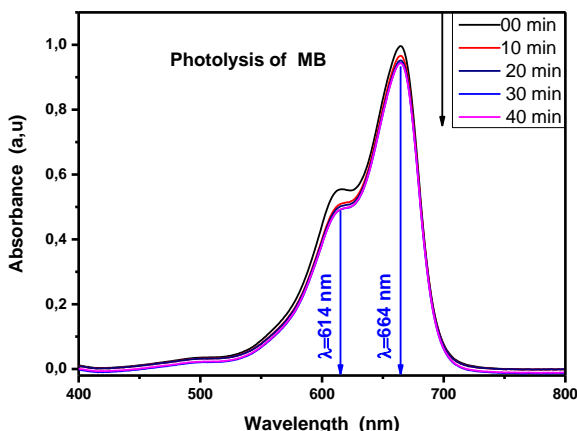


Figure V.2: Absorbance spectra of MB photolysis.

The degradation efficiency of MB was determined following the equation II.5:

$$D(\%) = \frac{A_0 - A_t}{A_0} \cdot 100 \quad \text{II.5}$$

The degradation was found to be less than 5.5% and consequently can be neglected (Fig.V.3).

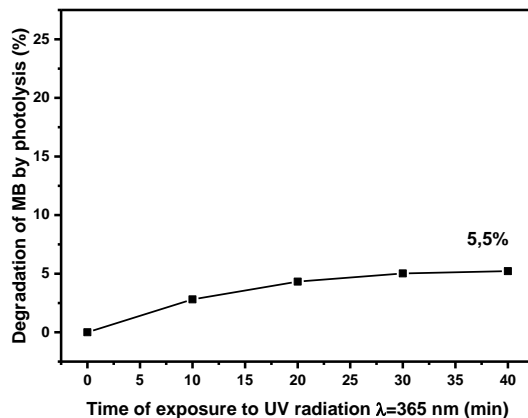


Figure V.3: Degradation of MB by photolysis as a function of time exposure to UV irradiation ($\lambda=365$ nm).

V.2- Study of adsorption effect of pure CuO and Sr doped CuO powders:

In order to assess the adsorption effect of MB by non-doped and Sr doped CuO powders, we added 0.4 g of powders to the MB solution ($5 \cdot 10^{-6}$ Mol). The obtained mixtures were subjected to

ultrasounds for 5 min, and then kept in the dark under magnetic stirring for 60 min. After each interval of 10 min, 8 ml were withdrawn from the solutions and the nanoparticles of pure CuO or Sr doped CuO were separated from MB solution by centrifugation. UV-Vis absorbance spectra were subsequently carried out on the various solutions obtained. The recorded spectra for the pure CuO powder are shown in figure V.4.

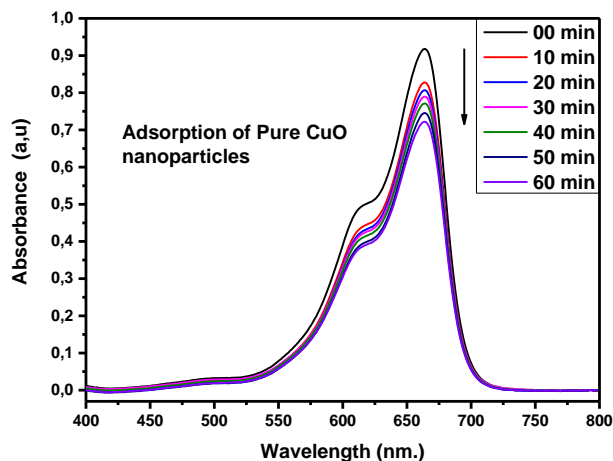


Figure V.4: MB absorbance spectra by adsorption of pure CuO nanoparticles.

The obtained spectra show a decrease in the absorption with time stirring in correlation with adsorption of MB molecules by pure CuO nanoparticles.

The curve representing the degradation rate as a function of stirring time in dark shows a degradation rate equal to 21,26% after 60 min (Fig.V.5).

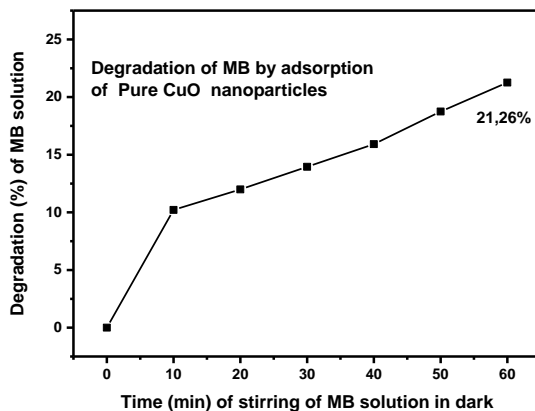


Figure V.5: MB degradation rate by adsorption of pure CuO nanoparticles.

The adsorption effect was also observed in the case of Sr doped CuO powders. Hence, figures V.6-8 reveal a clear degradation of MB compound in the solution with the stirring time, on the other hand, the corresponding curves (of degradation) reveal, at the beginning, an increase in the degradation of MB with added Sr. on the contrary, in the case of CuO + 5% Sr powder, the degradation of MB after 60 min, manifestly, decrease in comparison with those obtained in lower doped powders.

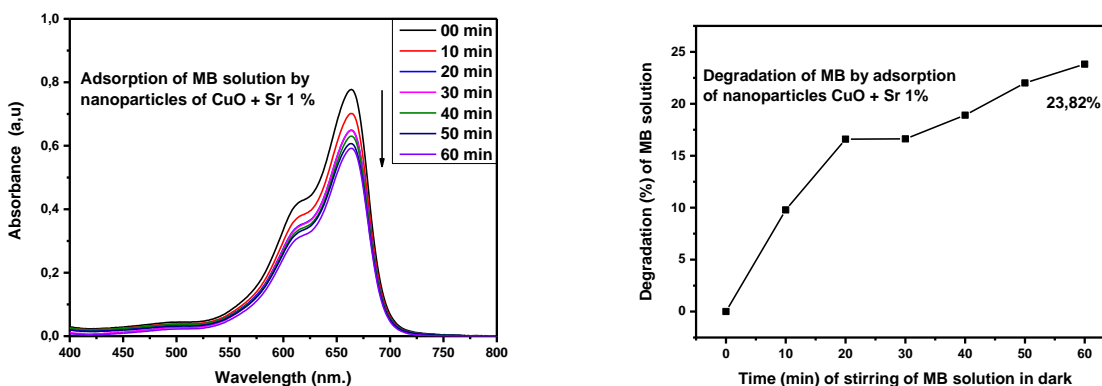


Figure V.6: MB Absorbance spectra and degradation rate by adsorption of CuO + 1% Sr nanoparticles.

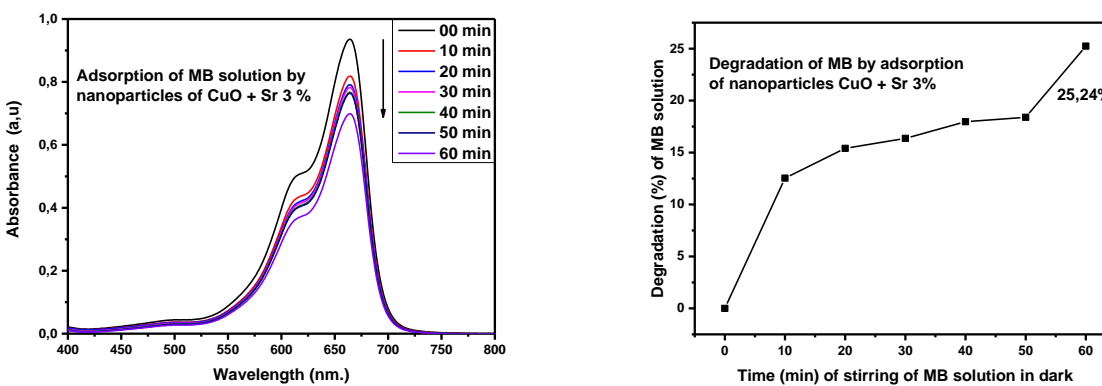


Figure V.7: MB Absorbance spectra and degradation rate by adsorption of CuO + 3% Sr nanoparticles.

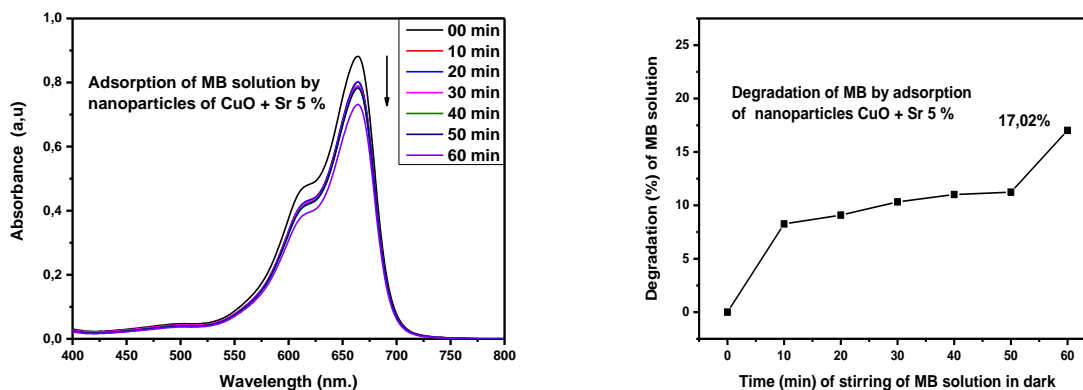


Figure V.8: MB Absorbance spectra and degradation rate by adsorption of CuO + 5% Sr nanoparticles

There are three main antagonist factors which can influence the adsorption of MB molecules by CuO nanopowders doped with Sr, On the one hand, the specific surface of the powders and the density of the dislocations which promote adsorption and on the other hand the secondary SrO phase which can on the contrary affects the adsorption. We have seen above that the specific surface area decreases as a function of the additions of Sr to reach its minimum in the case of 3% Sr doped CuO powders, it increases again in powders containing 5% Sr. The density of dislocations as a function of the additions in Sr evolves in the opposite direction: it is maximum in powders containing 1% Sr and decreases in the more loaded powders. Finally, the proportion of the CuO phase in the powders is of course a decreasing function of Sr percentage additions. The complex combination of these three parameters induces a complex evolution of the degradation of MB as a function of the addition of Sr. So, we obtain a maximum of adsorption in the case of 3% Sr doped powder and a minimum in the 5% Sr doped CuO powder.

V.3- Study of Photocatalytic Effect of Pure CuO and Sr Doped CuO powders:

The MB solutions containing pure CuO nanoparticles were exposed to UV radiation ($\lambda = 365$ nm) for different exposure times and then subjected to absorbance measurements. The obtained spectra are shown in figure V.9:

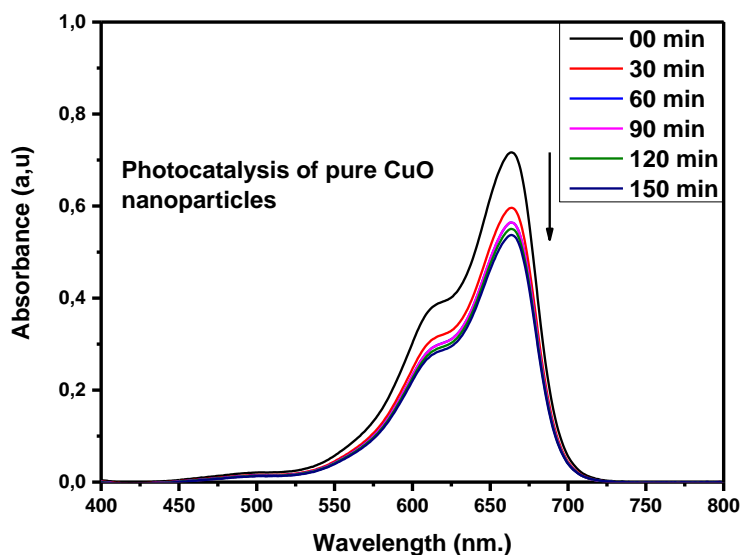


Figure V.9: MB absorbance spectra by adsorption of pure CuO nanoparticles.

We notice from these spectra that pure CuO powders have an obvious effect on the degradation of the MB dye. The photocatalytic effect is especially important in the first thirty minutes, in this step 17 % of MB compound degrades (Fig.V.10). After this, the degradation rate obviously decreases and only about 12 % of MB degradation is reached after 120 min.

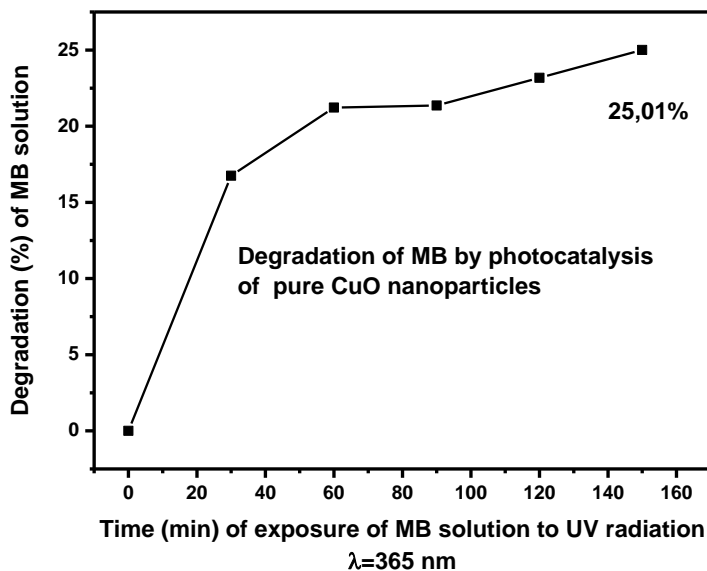


Figure V.10: MB degradation rate by photocatalysis of pure CuO nanoparticles.

In figures V.11-13 we reported the absorbance spectra and the corresponding rate degradation curves obtained from solution containing different Sr doped CuO powders and exposed to UV radiation for different times.

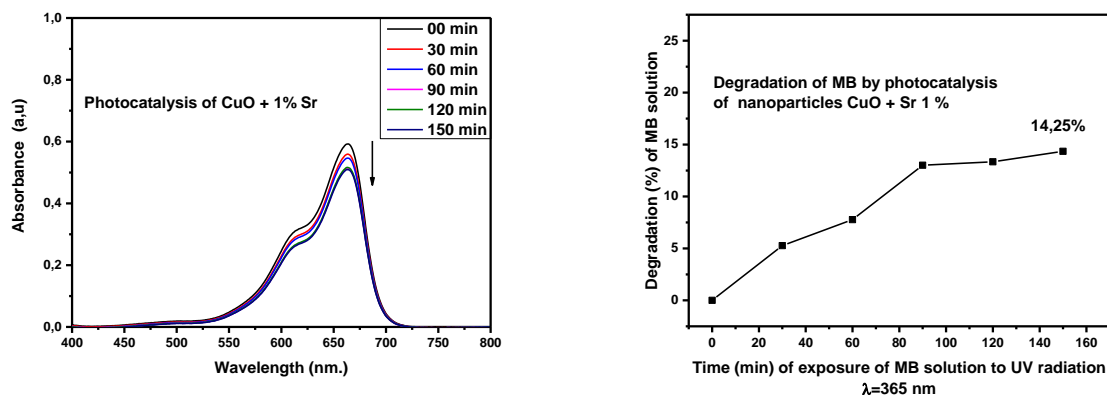


Figure V.11: MB Absorbance spectra and degradation rate by photocatalysis of CuO + 1% Sr nanoparticles.

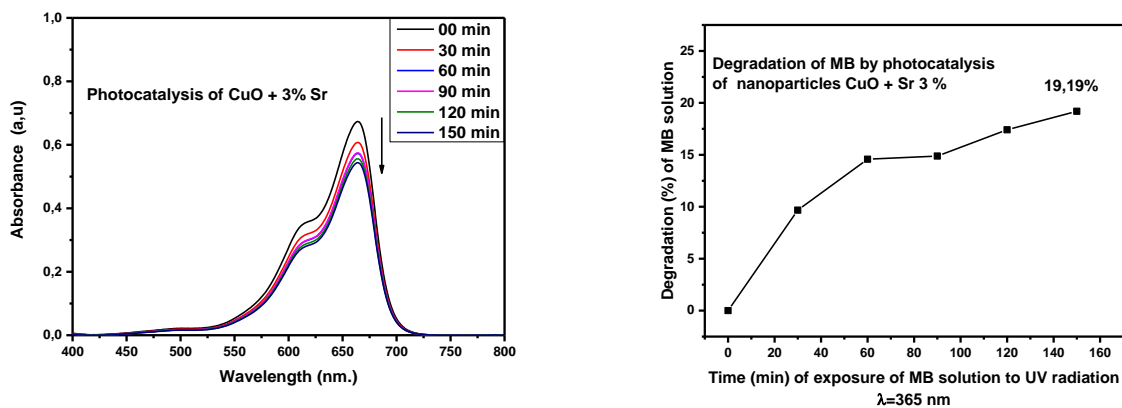


Figure V.12: MB Absorbance spectra and degradation rate by photocatalysis of CuO + 3% Sr nanoparticles.

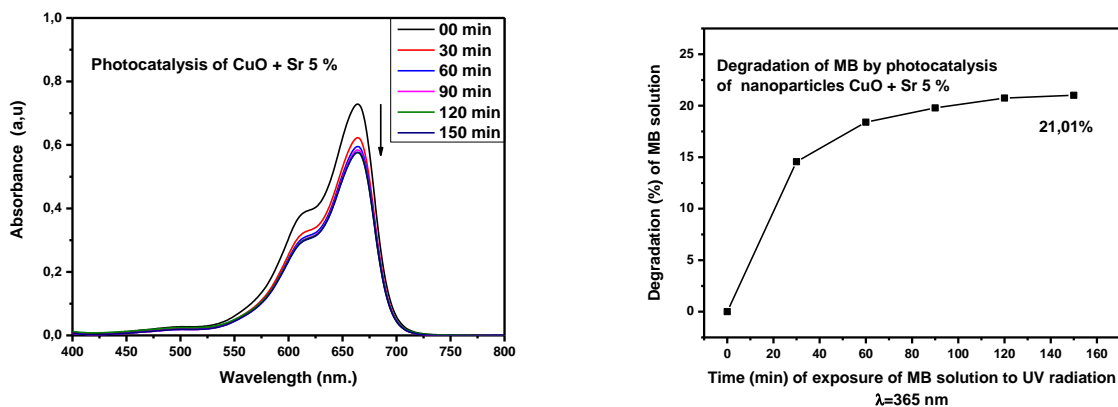


Figure V.13: MB Absorbance spectra and degradation rate by photocatalysis of CuO + 5% Sr nanoparticles.

It can be concluded from the different curves that Sr had, rather, a negative effect on CuO photocatalytic behavior. For example, the degradation rate decreases from 25.01% in Pure CuO powder to 14.35 in CuO+1% Sr powder. Such a result can be linked to the increase in the gap energy in doped CuO powder as a major factor. Nevertheless, others factors (specific surface, density dislocation and SrO phase proportion), as above mentioned, also affect the degradation evolution. These combined factors led to a complex evolution of the degradation rate as function of added Sr percentage (Tab.V.1).

Table V.1: MB total degradation rates by pure CuO and Sr doped CuO powders.

Catalyst	Degradation Rate by Adsorption (%)	Degradation Rate by Photocatalysis (%)	Total Degradation Rate (%)
Pure CuO	21.26	25.01	46.27
CuO + Sr 1%	23.82	14.35	38.17
CuO + Sr 3%	25.24	19.19	44.43
CuO + Sr 5%	17.02	21.01	38.03

VI- General Conclusion:

In this study, we synthesized pure and Sr doped CuO nanoparticles by the hydrothermal process. We used as precursor copper acetate, CuSO_4 of high chemical purity, a base NaOH, and Strontium chloride for doping. The synthesis of the pure or doped CuO nanoparticles was carried out in a sealed autoclave under normal temperature and pressure conditions, then heated to 200°C and maintained at this temperature for 2 hours. The obtained powders were washed and then dried at 80°C for 18h. X-ray spectra recorded from the various powders at room temperature revealed the formation of the monoclinic CuO phase belonging to the symmetry group $C2/c$ and the total absence of the Cu_2O phase. In the case of the powders doped with Sr, the XRD spectra revealed, at the same time, the formation of a secondary phase SrO whose proportion increases as a function of the Sr additions. The study of the shift and the variation of the amplitude of the diffracted peaks showed a limited solubility of Sr^{2+} cation in the CuO lattice. Crystallite sizes calculated from different spectra using two methods; the Scherrer and the Williamson-Hall methods respectively. The obtained results reveal the formation of CuO crystallites in nanometric scale. Moreover, the sizes of the crystallites increase slightly with the additions of Sr. In addition, size calculations by the Scherrer method showed anisotropic growth of the particles; the particles formed are more elongated in the [001] direction. X-rays diffraction study also allowed us to approximate the density of dislocations within the formed nanoparticles. Calculations based on the method proposed by Williamson and Smallman gave dislocation density values around 10^{15} m^{-2} , which corresponds to densities greater than those generally obtained in cold-worked metals, hence, it can be concluded that our powders contain a high dislocation density. This characteristic can be beneficial for the photocatalysis of powders since the structural defects are generally the site of the reactions between the crystal and the surrounding medium. Or, they can be a major obstacle when they become the site of recombination between photo-generated electrons and holes. The last important characteristic established from the results of X-ray diffraction is the specific surface per gram. The areas were calculated assuming different shapes of the nanoparticles (spherical, cylindrical, and prismatic). The areas calculated in the case of cylindrical or prismatic particles are relatively larger than those calculated in the case of spherical particles. They remain, however, of the same size order, i.e. a few tens of m^2 per g. Such a surface, logically allows good reactivity of the elaborated powders with the surrounding medium.

Conclusion

The spectra carried out by Fourier transform infrared spectrometry (FTIR) confirmed the formation of the pure CuO phase in pure powder and of the secondary SrO phase in doped powders. The shift in absorption bands of the CuO phase in this case reflects the effect of quantum confinement of infrared waves by the nanoparticles. The UV-visible absorbance spectra carried out on the different powders (pure and Sr doped CuO) showed a maximum absorption around 376 nm. The position of the absorption maximum (which corresponds to the absorption edge band) is slightly affected by the Sr doping, which again confirms the rather limited solubility of the Sr⁺² cation in the CuO phase. The calculation of the optical gap from UV-vis spectra, by the Tauc method showed a direct gap with values between $E_g = 1,624$ eV for the pure CuO powder and $E_g = 1,698$ eV for the 5% Sr doped CuO powder. These values are close to those found by several authors but greater than that corresponding to massive CuO samples, due to the quantum confinement of optical waves by nanoparticles.

Investigation of degradation by photolysis of Methylene Blue solution ($5 \cdot 10^{-5}$ Mol) using absorbance spectra revealed the two well-known absorbance peaks of MB at 613 and 664 nm respectively. The spectra carried out on solutions subjected for different exposure times (up to 40 min) to UV radiation ($\lambda = 365$ nm) showed a quite high stability of the MB solution.

The absorbance measurement carried out on MB solutions containing pure or doped powders respectively and mixed for different times using a magnetic bar. The obtained results show a decrease in the absorption with time stirring in correlation with adsorption of MB molecules by pure CuO and Sr doped CuO nanoparticles. In the case MB solution containing pure CuO powder the degradation rate attended 21,26% after 60 min. On the other hand, the obtained results reveal, at the beginning, an increase in the degradation of MB with added Sr. on the contrary, in the case of CuO + 5% Sr powder, the degradation of MB after 60 min, manifestly, decrease in comparison with those obtained in lower doped powders.

Finally, testes absorbance carried out on MB solutions containing different powders and submitted to UV radiation revealed a maximum of photocatalytic degradation in solution containing pure CuO powders. The degradation of MB compound decreases in the case of solutions containing doped powders. Nevertheless, the evolution of the degradation rate as function of added Sr is very complex due to the number of antagonist factors (band gap, specific surface, dislocation density, secondary SrO phase proportion) which influence the photocatalytic effect.

References

VII- References:

- [1] FUJISHIMA, A., & HONDA, K. (1972). Electrochemical Photolysis of Water at a Semiconductor Electrode. *Nature*, 238(5358), 37–38.
- [2] J.M. Herrmann, Heterogeneous photocatalysis: fundamentals and applications to the removal of various types of aqueous pollutants, *J. Catal. Today* 53 (1999) 115–129.
- [3] P.C. Maness, S. Smolinski, D.M. Blake, Z. Huang, E.J. Wolfrum, W.A. Jacoby, Bactericidal activity of photocatalytic TiO₂ reaction: toward an understanding of its killing mechanism, *Appl. Environ. Microbiol.* 65 (1999) 4094–4098.
- [4] Z. Huang, P.C. Maness, D. Blake, E.J. Wolfrum, S.L. Smolinski, W.A. Jacoby, Bactericidal mode of titanium dioxide photocatalysis, *J. Photochem. Photobiol. A* 130 (2000) 163–172.
- [5] D.S. Bhathkande, D.S. Pangarkar, A.ACM. Beenackers, Photocatalytic degradation for environmental applications—a review, *J. Chem. Technol.* 77 (2001) 102–116.
- [6] J.K. McCusker, Fuel from Photons, *Science* 293 (2001) 1599.
- [7] X. Zhang, D. Zhang, X. Ni, H. Zheng, Optical and electrochemical properties of nanosized CuO via thermal decomposition of copper oxalate, *Solid-State Electronics* 52 (2008) 245–248.
- [8] M.A. Dar a, Y.S. Kim b, W.B. Kim a, J.M. Sohn c, H.S. Shin b, Structural and magnetic properties of CuO nanoneedles synthesized by hydrothermal method, *Applied Surface Science* 254 (2008) 7477–7481.
- [9] Doerfler W, Hauffe K (1964) Heterogeneous photocatalysis II. The mechanism of the carbon monoxide oxidation at dark and illuminated zinc oxide surfaces. *J Catal* 3:171–178.
- [10] Jean-Marie Herrmann, Heterogeneous photocatalysis: fundamentals and applications to the removal of various types of aqueous pollutants, *Catalysis Today* 53 (1999) 115–129.
- [11] Harada, K., Hisanaga, T., & Tanaka, K. (1990). Photocatalytic degradation of organophosphorus insecticides in aqueous semiconductor suspensions. *Water Research*, 24(11), 1415–1417.
- [12] A. Nezamzadeh-Ejehieh and Z. Salimi, Heterogeneous photodegradation catalysis of o-phenylenediamine using CuO/X zeolite, *Applied Catalysis A: General* 390 (2010) 110-118.
- [13] Umar, M., & Abdul, H. (2013), Photocatalytic Degradation of Organic Pollutants in Water. *Organic Pollutants - Monitoring, Risk and Treatment*.
- [14] Chong M.N., Jin B., Chow C.W.K., Saint C. Recent Developments in Photocatalytic Water Treatment Technology: A Review. *Water Resources* 2010 (44) 2997-3027.
- [15] Aracely Hernández-Ramírez, Iliana Medina-Ramírez, Photocatalytic Semiconductors Synthesis, Characterization, and Environmental Applications.
- [16] Wang Y, Wang Q, Zhan X, Wang F, Safdar M, He J (2013) Visible light driven type II hetero structures and their enhanced photocatalysis properties: a review. *Nanoscale* 5:8326–8339.
- [17] Guillard C., Lachheb H., Houas A., Elaloui E., Hermann J-M. Influence of Chemical Structure of Dyes, of pH and of Inorganic Salts on their Photocatalytic Degradation by TiO₂ Comparison of the Efficiency of Powder and Supported TiO₂. *Journal of Photochemistry and Photobiology A: Chemical* 2003 (158) 27-36.

References

- [18] Gaya U.I., Abdullah A.H. Heterogeneous Photocatalytic Degradation of Organic Contaminants over Titanium Dioxide: A Review of Fundamentals, Progress and Problems. *Journal of Photochemistry and Photobiology C Photochemistry Reviews* 2008 (9) 1-12.
- [19] Kogo K., Yoneyama H., Tamura H. Photocatalytic oxidation of cyanide on platinized titanium dioxide. *The Journal of Physical Chemistry* 1980 (84) 1705–1710.
- [20] Chong M.N., Jin B., Chow C.W.K., Saint C. Recent Developments in Photocatalytic Water Treatment Technology: A Review. *Water Resources* 2010 (44) 2997-3027.
- [21] Saquib M., Muneer M. TiO₂-mediated Photocatalytic Degradation of a Triphenyl Methane Dye (Gentian Violet), in Aqueous Suspensions. *Dyes and Pigments* 2003(56) 37-49.
- [22] Roduner E (2006) Size matters why nanomaterials are different. *Chem Soc Rev* 35(7):583–592
- [23] M. Mansoob Khan, D. Pradhan and Y. Sohn, Nanocomposites for Visible Light-induced Photocataly, *Crystallographica Section B Structural Crystallography and Crystal Chemistry*, 26(1), 8–15.
- [24] Åsbrink, S., & Norrby, L. J. (1970). A refinement of the crystal structure of copper(II) oxide with a discussion of some exceptional e.s.d.'s. *Acta*.
- [25] H. Siddiqui Mohammad, R. Parra Padmini Pandey M.S. Qureshi, and Fozia Z. Haque, Performance evaluation of optimized leaf-shaped two-dimension (2D) potassium doped CuO nanostructures with enhanced structural, optical and electronic properties, *Ceramics International* Volume 46, Issue 12, 15 August 2020, Pages 20404-20414.
- [26] Koffyberg, F. P., & Benko, F. A. (1982). A photoelectrochemical determination of the position of the conduction and valence band edges of p-type CuO. *Journal of Applied Physics*, 53(2), 1173–1177.
- [27] B. K. Meyer, A. Polity, D. Reppin, M. Becker, P. Hering, P. J. Klar, Th. Sander, C. Reind, J. Benz, M. Eickhoff, C. Heiliger, M. Heinemann, J. Blaßing, A. Krost, S. Shokovets, C. Müller, and C. Ronning, Binary copper oxide semiconductors: From materials towards devices, *Phys. Status Solidi B*, 1–23 (2012).
- [28] Munirathinam Elavarasan I and Thomas Chung-Kuang Yang. Facile Synthesis Protocol to the Preparation of Strontium Doped Copper Oxide for the Electrochemical Glucose Sensor, *Int. J. Electrochem. Sci.*, 14 (2019) 2914 – 2924.
- [29] Rahman, M. M., Hussain, M. M., & Asiri, A. M. (2016). A novel approach towards hydrazine sensor development using SrO·CNT nanocomposites. *RSC Advances*, 6(70), 65338–65348.
- [30] Langford, J. I., & Wilson, A. J. C. (1978). Scherrer after sixty years: A survey and some new results in the determination of crystallite size. *Journal of Applied Crystallography*, 11(2), 102–113.
- [31] Pielaszek R. (2003) Diffraction studies of microstructure of nanocrystals exposed to high pressure. Ph.D. thesis, Warsaw University.
- [32] J. I. Langford and D. Louër, High-Resolution Powder Diffraction Studies of Copper(II) Oxides, *J. Appl. Cryst.* (1991).24, 149-155.
- [33] C. Suryanarayana and M. Grant Norton; « X-Ray Diffraction A Practical Approach », Springer et Sciences +Business Media, New York, 1998.

References

- [34] G. K. Williamson and W. H. Hall, "X-ray Line Broadening from Filed Aluminium and Wolfram," *Acta Metall.*, Vol. 1, 1953, pp. 22-3.
- [35] Sneha Upadhyay a, Kinnari Parekh b, Brajesh Pandey a, *, Influence of crystallite size on the magnetic properties of Fe₃O₄ nanoparticles, *Journal of Alloys and Compounds* 678 (2016) 478e485.
- [36] Rita John¹, Rajaram Rajakumari, Synthesis and Characterization of Rare Earth Ion Doped Nano ZnO, *Nano-Micro Lett.* 4 (2), 65-72 (2012).
- [37] Williamson, G. K., & Smallman, R. E. (1956). III. Dislocation densities in some annealed and cold-worked metals from measurements on the X-ray debye-scherrer spectrum. *Philosophical Magazine*, 1(1), 34–46.
- [38] M. Saleem, L. Fang, H. B. Ruan, F. Wu¹, Q. L. Huang, C. L. Xu and C. Y. Kong, Effect of zinc acetate concentration on the structural and optical properties of ZnO thin films deposited by Sol-Gel method, *International Journal of Physical Sciences* Vol. 7(23), pp. 2971-2979, 15 June, 2012.
- [39] Jeong, H. Y., Lee, J. H., & Hayes, K. F. (2008). Characterization of synthetic nanocrystalline mackinawite: Crystal structure, particle size, and specific surface area. *Geochimica et Cosmochimica Acta*, 72(2), 493–505.
- [40] Hafsa Siddiqui, Mohammad Ramzan Parra, M. S. Qureshi, M. M. Malik, and Fozia Z. Haque, Studies of structural, optical, and electrical properties associated with defects in sodium-doped copper oxide (CuO/Na) nanostructures, Springer Science + Business Media, LLC, part of Springer Nature 2018.
- [41] Kliche, G., & Popovic, Z. V. (1990). Far-infrared spectroscopic investigations on CuO. *Physical Review B*, 42(16), 10060–10066.
- [42] H. Hagemam, H. Bill, W. Sadowski, E. Walker and M. François, RAMAN SPECTRA OF SINGLE CRYSTAL CuO, *Solid State Communicatlon*, Vol. 73. No. 6, pp. 447-451, 1990.
- [43] Singh, J., Kumar, V., Kim, K.-H., & Rawat, M. (2019). Biogenic synthesis of copper oxide nanoparticles using plant extract and its prodigious potential for photocatalytic degradation of dyes. *Environmental Research*, 108569.
- [44] Dar, M. A., Kim, Y. S., Kim, W. B., Sohn, J. M., & Shin, H. S. (2008). Structural and magnetic properties of CuO nanoneedles synthesized by hydrothermal method. *Applied Surface Science*, 254(22).
- [45] A. Asha Radhakrishnan, B. Baskaran Beena, Structural and Optical Absorption Analysis of CuO Nanoparticles, *Indian Journal of Advances in Chemical Science* 2 (2) (2014) 158-161.
- [46] Siddiqui, H., Qureshi, M. S., & Haque, F. Z. (2016). Hexamine (HMT) assisted wet chemically synthesized CuO nanostructures with controlled morphology and adjustable optical behavior. *Optical and Quantum Electronics*, 48(7).
- [47] Rahman, M. M., Hussain, M. M., & Asiri, A. M. (2016). A novel approach towards hydrazine sensor development using SrO· CNT nanocomposites. *RSC Advances*, 6(70), 65338–65348.
- [48] Zhao, X., Wang, P., Yan, Z., & Ren, N. (2015). Room temperature photoluminescence properties of CuO nanowire arrays. *Optical Materials*, 42, 544–547.

References

- [49] Willardson RK, Beer AC (1967), *Semiconductor and semimetals: optical properties of III-V compounds*, vol 3, Academic press, New York
- [50] H. Tang, K. Prasad, R. Sanjinès, P.E. Schmid, and F. Lèvy: *J.App.Phy.*, 75- 4, (1994) 2042.
- [51] Wang, Y., Jiang, T., Meng, D., Kong, J., Jia, H., & Yu, M. (2015). Controllable fabrication of nanostructured copper compound on a Cu substrate by a one-step route. *RSC Advances*, 5(21), 16277–16283.
- [52] Prabu, R. D., Valanarasu, S., Kulandaisamy, I., Ganesh, V., Shkir, M., & Kathalingam, A. (2017). Studies on copper oxide thin films prepared by simple nebulizer spray technique. *Journal of Materials Science: Materials in Electronics*, 28(9), 6754–6762.
- [53] Marabelli, F., Parravicini, G. B., & Salghetti-Drioli, F. (1995). Optical gap of CuO. *Physical Review B*, 52(3), 1433–1436.

Annex:

Specific surface in the case of spherical nanoparticles:

The specific surface in the case of homogeneous spherical particles assuming that D represents the diameter of the particle. Under these conditions the area of each particle is given by:

$$S_p = \pi D^2$$

its volume is given by:

$$V_p = \frac{\pi}{6} D^3$$

and the mass of each particle is simply equal to:

$$m_p = \rho \frac{\pi}{6} D^3$$

The number of particles per gram is, in this case, equal to:

$$n_p = \frac{6}{\rho \pi D^3}$$

Hence a total surface (specific surface):

$$S = n_p S_p = \frac{6}{\rho \pi D^3} 4D^2 = \frac{6}{\rho D}$$

Relation that we modify slightly by writing the unit of density as follows:

$$\rho = \frac{g}{nm \cdot m^2 \cdot 10^3}$$

We obtain, then, the following expression:

$$S = \frac{6 \cdot 10^3}{D * \rho}$$

Specific surface in the case of cylindrical particles:

If we assume that the particles have a cylindrical shape (rod) whose generatrix is D_c and the diameter of the base is D_a , the surface of the particle will in this case be given by:

$$S_p = \left(\pi D_a D_c + \pi \frac{D_a^2}{2} \right)$$

The volume of the particle is given by:

$$V_p = \frac{\pi}{4} D_a^2 D_c$$

hence the mass of a particle:

$$m_p = \rho \frac{\pi}{4} D_a^2 D_c$$

The number of particles per gram is, equal to:

$$n_p = \frac{4}{\rho \pi D_a^2 D_c}$$

So, a total surface (specific surface):

$$S = n_p S_p = \frac{(2D_a + 4D_c)}{\rho D_a * D_c}$$

Specific surface in the case of prismatic particles:

The specific surface in the case of prismatic particles assuming that D_a , D_b and D_c correspond respectively to the particle sizes in the three main directions, the surface of the particle will in this case be given by:

$$S_p = 2D_a D_b + 2D_b D_c + D_a D_c \sin \theta$$

its volume is given by:

$$V_p = D_a D_b D_c \sin \beta$$

the mass of a particle:

$$m_p = \rho D_a D_b D_c \sin \theta$$

The number of particles per gram:

$$n_p = \frac{1}{\rho D_a D_b D_c \sin \theta}$$

We obtain, a total specific surface:

$$S = \frac{2}{\rho} \left(\frac{1}{D_a \sin \beta} + \frac{1}{D_c \sin \beta} + \frac{1}{D_b} \right)$$

Abstract

In this work, we synthesized Sr-doped copper oxide CuO nanoparticles by the hydrothermal process. Copper sulfate (CuSO_4) and strontium chloride (SrCl_2) have been used as precursor chemical compounds.

The characterization of the nanoparticles has been made using X-ray diffraction, infrared spectroscopy and UV-Vis spectroscopy.

Analyzes carried out using X-ray diffraction and infrared spectroscopy demonstrated the formation of the pure CuO phase as well as the SrO phase in the case of doped powders. The proportion of this last phase increases with the initial SrCl_2 additions.

Particle size approach from diffraction spectra data using both Scherrer's formula and Williamson-Hall deconvolution method confirmed a nanostructured particle (with a size varying between 13,71 and 18,66 nm by Scherrer and 27,13 and 40,78 nm by Williamson-Hall). The latter method also revealed residual strains of around 0.2%.

The obtained nanoparticles contained a quite higher density of dislocations of about 10^{15} m^{-2} . Furthermore, the estimated specific surface area of the nanoparticles (based on X-ray diffraction data and assuming different particle shapes) was in the order of a few tens of m^2 .

Tauc method used to approach the band gap of CuO phase showed a blue shift of the gap ($E_g \sim 1.74 \text{ eV}$) probably in consequence of the optic confinement by the nanoparticles.

Finally, testes absorbance carried out on MB solutions containing different powders and submitted to UV radiation revealed a maximum of photocatalytic degradation in solution containing pure CuO powders. The degradation of MB compound decreases in the case of solutions containing doped powders. Nevertheless, the evolution of the degradation rate as function of added Sr is very complex due to the number of antagonist factors (band gap, specific surface, dislocation density, secondary SrO phase proportion) which influence the photocatalytic effect.

Résumé

ÉTUDE DE L'ACTIVITÉ PHOTOCATALYTIQUE DE NANOMATÉRIAUX À BASE D'OXYDES MÉTALLIQUES SEMI-CONDUCTEURS

Dans ce travail, nous avons élaboré des nanoparticules de l'oxyde du cuivre CuO dopées en Sr par le procédé hydrothermal à partir du sulfate de cuivre (CuSO₄) comme précurseur et du chlorure de strontium (SrCl₂) pour le dopage des particules.

Pour la caractérisation des nanoparticules nous avons utilisé la diffraction des rayons X, la spectroscopie infrarouge et la spectroscopie UV-Vis.

Les analyses réalisées à l'aide de la diffraction des rayons X et de la spectroscopie infrarouge ont mis en évidence la formation de la phase CuO pure ainsi que la phase SrO dans le cas des poudres dopées. La proportion de cette dernière phase croît avec les additions initiales de SrCl₂.

Le calcul de la taille des particules à partir des données des spectres de diffraction en utilisant aussi bien la formule de Scherrer que la méthode de déconvolution de Williamson-Hall ont montré que ces particules sont nanométriques (avec une taille qui varie entre 13,71 et 18,66 nm par Scherrer et 27,13 et 40,78 nm par Williamson-Hall). Cette dernière méthode a révélé également des déformations résiduelles de l'ordre de 0.2%.

La densité des dislocations dans les particules est assez élevée, elle est de l'ordre de 10^{15} m^{-2} .

Par ailleurs, la surface spécifique des nanoparticules est estimée (sur la base des données de la diffraction des rayons X et en supposant différentes formes des particules) de l'ordre de quelques dizaines de m^2 .

Le calcul du gap optique par la méthode de Tauc a montré un décalage du gap vers le bleu ($E_g \sim 1.74 \text{ eV}$) en raison de la taille nanométrique des particules.

Enfin, les tests d'absorbance réalisés sur des solutions MB contenant différentes poudres et soumises au rayonnement UV a révélé un maximum de dégradation photocatalytique dans la solution contenant des poudres de CuO pures. La dégradation du composé MB diminue dans le cas de solutions contenant des poudres dopées. Néanmoins, l'évolution du taux de dégradation en fonction du Sr ajouté est très complexe du fait du nombre de facteurs antagonistes (bande interdite, surface spécifique, densité de dislocation, proportion de la phase secondaire SrO) qui influencent l'effet photocatalytique.

ملخص

دراسة نشاط التحفيز الضوئي للمواد النانومترية المكونة من أنصاف النواقل لأكاسيد المعادن

في هذا العمل ، قمنا بتصنيع جسيمات نانومترية من أكسيد النحاس المطعم بـ Sr بواسطة تقنية الهيدروترمال. تم استخدام كبريتات النحاس (CuSO_4) وكلوريد السترونتيوم (SrCl_2) كمركبات كيميائية أولية. تم توصيف الجسيمات نانومترية باستخدام حيود الأشعة السينية ، والتحليل الطيفي بالأشعة تحت الحمراء ، والتحليل الطيفي للأشعة المرئية وفوق البنفسجية.

أظهرت التحليلات التي أجريت باستخدام حيود الأشعة السينية والتحليل الطيفي للأشعة تحت الحمراء تشكيل الطور CuO النقي وكذلك طور SrO في حالة المساحيق المطعمة. تزداد نسبة هذا الطور مع الإضافات الابتدائية للمركب SrCl_2 . أكد حساب أبعاد الجسيمات بالإعتماد على معطيات حيود الأشعة السينية باستخدام كل من صيغة شيرير وطريقة ويليامسون- هول أن الجسيمات المحصل عليها ذات أبعاد نانومترية (يتراوح بعدها بين 13.71 و 18.66 نانومتر بواسطة شيرير و 13،27 و 40.78 نانومتر بواسطة ويليامسون-هول). كشفت هذه الطريقة الأخيرة أيضًا عن تشوهات متبقية تبلغ حوالي 0.2٪.

تحتوي الجسيمات النانومترية التي تم الحصول عليها على كثافة إنخلاعات من رتبة 10^{15}m^{-2} أو هي كثافة أعلى من تلك الموجودة عامة في المعادن المطرقة عند درجات الحرارة العادية.

علاوة على ذلك ، بلغت المساحة النوعية للجسيمات النانومترية (بناءً على بيانات حيود الأشعة السينية وافترض أشكال مختلفة للجسيمات) في حدود بضع عشرات من الأمتار المربعة.

أظهرت طريقة Tauc المستخدمة لتقدير طاقة النطاق الممنوع للطور CuO أنزياحًا نحو اللون الأزرق نتيجة للحجر الكمي للأشعة الضوئية بواسطة الجسيمات النانومترية.

أخيرًا ، كشفت تجارب الإمتصاص التي تم إجراؤها على محاليل MB تحتوي على مساحيق مختلفة عرضت للأشعة فوق البنفسجية عن حد أقصى من التحلل الضوئي للمركب MB في المحلول الذي يحتوي على مساحيق CuO نقية. في حين ينخفض تحلل مركب بروميد الميثيل في حالة المحاليل المحتوية على مساحيق مطعمة. ومع ذلك، فإن تطور معدل التحلل كدالة لإضافات Sr معقد للغاية بسبب عدد العوامل المضادة (فجوة النطاق ، المساحة النوعية، كثافة الإنخلاعات ، نسبة الطور الثانوي SrO) و التي تؤثر على التحليل الضوئي.